

POPSTAR Evolutionary Synthesis Models III: Photometric properties of young star clusters and mixed populations

M.L. García-Vargas¹ *, M. Mollá², and M.L. Martín-Manjón³

¹ *FRAC TAL SLNE, C/ Tulipán 2, p13, 1A, 28231 Las Rozas de Madrid, (Spain)*

² *Departamento de Investigación Básica, CIEMAT, Avda. Complutense 40, 28040, Madrid, (Spain)*

³ *Departamento de Física Teórica, Universidad Autónoma de Madrid. Cantoblanco. E-28049 Madrid. Spain.*

Accepted Received ; in original form

ABSTRACT

This is the third paper of a series reporting the results from the POPSTAR evolutionary synthesis models. The main goal of this work is to present and discuss the synthetic photometric properties of Single Stellar Populations (SSPs) resulting from our POPSTAR code. Colours in the Johnson and SDSS systems, H_α and H_β luminosities and equivalent widths, and ionising region size, have been computed for a wide range of metallicity ($Z = 0.0001 - 0.05$) and age (0.1 Myr to 20 Gyr). We calculate the evolution of the cluster and the region geometry in a consistent manner. We demonstrate the importance of the contribution of emission lines to broader-band photometry when characterising stellar populations, through the presentation of both contaminated and non-contaminated colours (in both the Johnson and SDSS systems). The tabulated colours include stellar and nebular components, in addition to line emission. The main application of these models is the determination of physical properties of a given young ionising cluster, when only photometric observations are available; for an isolated star forming region, the young star cluster models can be used, free from the contamination of any underlying background stellar population. In most cases, however, the ionising population is usually embedded in a large and complex system, and the observed photometric properties result from the combination of a young star-forming burst and the underlying older population of the host. Therefore, the second objective of this paper is to provide a grid of models useful in the interpretation of mixed regions where the separation of young and old populations is not sufficiently reliable. We describe the set of PopStar Spectral Energy Distributions (SEDs), and the derived colours for mixed populations where an underlying host population is combined in different mass ratios with a recent ionising burst. These colours, together with other common photometric parameters, such as the H_α radius of the ionised region, and Balmer line equivalent widths and luminosities, allow one to infer the physical properties of star-forming regions even in the absence of spectroscopic information.

Key words: galaxies: abundances – galaxies: evolution – galaxies: starburst – galaxies: stellar content

1 INTRODUCTION

For many years, broad-band photometry was used as the primary tool in deriving ages for both single bursts and mixed stellar populations. Broadly speaking, blue colours were taken to be indicative of young populations, while red colours were associated with older populations. Only dust was thought to complicate this picture, through the general reddening of the population. From an observational perspective, few works have considered the potential contaminating impact of gas emission upon broadband colours. For example, López-Sánchez & Esteban (2008) analysed carefully, colour-colour diagrams, taking into account this correction, and thereby

proposing a mechanism for separating the contribution from the underlying stellar population, starburst population, and line emission, for better quantitative comparison with evolutionary models of stellar populations. From a theoretical perspective, colours were calculated typically for the stellar component only or, in a few cases, by taking into account the nebular continuum. Only recently, several works (Martín-Manjón et al., 2008; Reines et al., 2010, and references therein) have started to quantify the role of line emission from ionised gas surrounding young star clusters in the contamination of broad-band colours. These latter authors examined two young massive clusters in NGC 4449, demonstrating that the contribution of both nebular continuum and line emission is essential to reproduce the observed broad-band fluxes. The comparison of model spectral energy distributions with and without nebular con-

* e-mail:marisa.garcia@fractal-es.com

tinuum and/or emission lines shows that the inferred stellar mass can change by up to a factor of ~ 2.5 , depending upon the filter in question. Atek et al. (2011) also find that nebular lines can contaminate the total broadband flux by ~ 0.3 mag (median, but up to ~ 1 mag, in certain cases). This effect is important since low-redshift galaxies with active star formation may mimic the colour-selection criteria used in some high-redshift dropout surveys. This potential impact on the mass and age of galaxies is also important for cosmological studies which use these values as clues to disentangling the temporal history of galaxy assembly. Despite this importance, to our knowledge there is no available systematic grid of models which includes the effect of emission lines on broadband colours spanning a wide range in age and metallicity. Our work has been designed to fill this gap.

Over the past two decades, a wealth of powerful ground-based facilities, particularly in the visible, has driven the use of spectroscopic techniques to infer the underlying physical properties of ionising star clusters. High signal-to-noise spectra were required, in order to derive the nebular electron density and electronic temperature, and from these gas parameters, the abundance content. In the absence of a consistent grid of models against which to compare, photometric information has not been used as the main tool for deriving star-forming properties. In terms of observations, there were few consistent samples of HII regions (or small to medium-size star-forming objects) that would allow us to test models and from which we could extract statistical conclusions. Moreover, these existing observational samples were usually biased towards bright and low-to-intermediate metallicity regions. This subject has been exhaustively discussed by Martín-Manjón et al. (2010, hereinafter Paper II), in which we presented the emission line spectra for our models as a function of the physical properties of the ionising clusters and compared the resulting diagnostic diagrams with a complete spectroscopic sample of HII regions for which abundances were derived consistently using an appropriate empirical calibration.

The recent generation of deep surveys, taken with mid-to-large aperture telescopes, have now released complete photometric catalogues of star forming regions and galaxies at different redshifts. This has motivated us to deliver a set of models which can aid in the derivation of the physical properties of stellar populations, without the necessity of spectroscopic data. With this in mind, we have computed the colours and other common photometric parameters, such H_α radius, H_α and H_β equivalent widths and H_α and H_β luminosities. We are convinced that these models will be a powerful tool in the interpretation of star-forming region photometric data, providing the means to infer their mass, age, and metallicity when embedded within more complex and evolved systems.

We have computed colours previously with the PopSTAR SEDs in both Johnson and SDSS systems (Mollá et al, 2009, hereafter, Paper I). We present now the colour evolution of star forming regions formed by a SSP, including the contribution of the strongest emission lines from the ionised nebula, which can be used to derive the physical properties of the ionising clusters. These SSP models can be used directly to compare with specific, usually small and detailed, photometric samples, where colours have been corrected for the contamination from an underlying population. However, this is not the general case, since the subtraction of the underlying population delivers results that are not always reliable; furthermore, this approach is not the most commonly used one when a large amount of data, like the output of extremely large surveys, are analysed. Such surveys are used to obtain statistical conclusions about the star forming regions, and therefore the use of appropriate theoretical models is essential. For this reason, in addition to the SSP mod-

els, we have also computed a complete set of photometric properties for mixed populations, to simulate local star-forming regions embedded in more complex star systems. These models are particularly useful when the subtraction of an underlying population is not sufficiently reliable.

This paper describes the photometrical model and demonstrates how photometry can be an alternative and powerful tool in the delivery of inferred ages and metallicities for star forming regions, as well as how it can give an estimation of the mass-ratio of the star-forming region to that of the underlying population. The models presented here are applicable to nearby/local star forming regions only, since the contribution of the emission lines varies with redshift. It is obvious that the most important emission lines contaminate different filters, with different transmittance, as a function of redshift. We outline the importance of an extension of this work to higher redshift, to study the impact of emission lines on broadband photometry of samples at different redshift. Dust re-emission and near-IR photometry will be also included to extend the use of the models to large samples covering a wide range of redshifts.

Section 2 summarises the main properties of the grid of evolutionary synthesis models used to compute the magnitudes of pure SSPs, the method to calculate the emission line intensities of the photo-ionised nebula and, consequently, the associated contaminated colours. Section 3 presents and analyses the results of our models for young ionising SSPs. These models can be used for deriving the physical properties of the ionising populations in regions whose observed colours have been previously de-contaminated from the underlying populations. Section 4 describes the set of models for mixed populations, applicable to characterising star-forming regions where these bursts are placed on an underlying population and where we cannot separate both components observationally. Finally, Section 5 summarises our results.

2 SSP COLOUR CALCULATIONS

2.1 PopSTAR Model Summary

A detailed description of PopSTAR can be found in Paper I. PopSTAR provides a set of evolutionary synthesis models for SSPs, covering a wide range in age and metallicity. The basic grid is composed of SSPs for six different initial mass functions (IMFs). For this work, we have used only a Salpeter IMF (Salpeter, 1955) with lower and upper mass limits of 0.15 and $100 M_\odot$, respectively. We have not included binaries nor mass segregation.

The isochrones employed are updated versions of those from Bressan et al. (1998) for six metallicities: $Z = 0.0001, 0.0004, 0.004, 0.008, 0.02$, and 0.05 . The use of very low metallicity models ($Z=0.0001$) was not included in comparable work prior to that of PopSTAR. The age ranges from $\log \tau = 5.00$ to 10.30 with a variable time resolution reaching $\Delta(\log \tau) = 0.01$ in the youngest populations. Again, details of the isochrones are described in Paper I.

Stellar atmosphere models are taken from Lejeune, Cuisinier & Buser (1997), due to its expansive coverage in effective temperature, gravity, and metallicities, for stars with $T_{\text{eff}} \leq 25000\text{K}$. For O, B, and WR stars, the NLTE blanketed models of Smith, Norris & Crowther (2002) (for metallicities $Z = 0.001, 0.004, 0.008, 0.02$, and 0.04) are used. There are 110 models for O-B stars, calculated by Pauldrach, Hoffmann & Lennon (2001), with $25000\text{K} < T_{\text{eff}} \leq 51500\text{K}$ and $2.95 \leq \log g \leq 4.00$, and 120 models for WR stars (60 WN and 60 WC), from Hillier & Miller (1998), with $30000\text{K} \leq T^* \leq 120000\text{K}$ and $1.3 R_\odot \leq R^* \leq 20.3 R_\odot$ for WN, and with

$40000\text{ K} \leq T^* \leq 140000\text{ K}$ and $0.8 R_\odot \leq R^* \leq 9.3 R_\odot$ for WC. T^* and R^* are the temperature and the radius at a Roseland optical depth of 10. The assignment of the appropriate WR model is consistently made by using the relationships between opacity, mass loss, and velocity wind, as described in Paper I. For post-AGB and planetary nebulae (PN) with T_{eff} between 50000 K and 220000 K, the NLTE models from Rauch (2003) are taken. For higher temperatures, POPSTAR uses black-bodies. The use of these latter models modifies the resulting intermediate age SEDs.

For each cluster, the total mechanical energy from stellar winds and supernova has been calculated. We have used this mechanical energy to calculate the HII region's inner radius (see §2.2). We have also computed the nebular continuum emission from hydrogen and helium (He and He⁺) free-free, free-bound, and 2-photon continuum emission.

The SEDs (stellar+nebular) corresponding to the six metallicities and ages up to 20 Myr have been introduced to the photo-ionisation code CLOUDY (Ferland et al., 1998) to obtain the emission line spectra (see Paper II for details). We take seven possible cluster masses: 1.2×10^4 , 2.0×10^4 , 4.0×10^4 , 6.0×10^4 , 1.0×10^5 , 1.5×10^5 and $2.0 \times 10^5 M_\odot$ selected to cover the H_α luminosity range observed for medium-to-large HII regions. The gas surrounding the cluster is assumed to have the same chemical composition as the stars of the cluster. For each metallicity, the element abundances heavier than helium have been scaled by a constant factor, with respect to the hydrogen content, according to the solar abundances from Grevesse & Sauval (1998) and depleted when necessary (see Table 2 from Paper II). The models assume a bubble geometry, with an ionised bounded nebula whose size is given by the cluster evolution. Therefore, the internal radius of the shell is the distance at which the ionised gas is deposited in that nebula by the cluster's mechanical energy. Be aware that the observed radius of an HII region is not necessarily the inner radius of the ionised region (see §2.2). The effect of dust here has not been included.

The hydrogen density has been considered constant throughout the nebula and equal to the electron density for complete ionisation. We have generated models assuming two different values of electron density, n_H : 10 cm^{-3} and 100 cm^{-3} , in order to quantify the impact of density on the emitted spectrum. A density of 10 cm^{-3} is more appropriate for small-medium isolated HII regions while 100 cm^{-3} is more appropriate for HII galaxies, large circumnuclear HII regions, often found around the nuclei of starbursts, or AGN. Although the constant density hypothesis is not realistic when detailed nebular studies are done, it can be considered representative when the integrated spectrum of the nebula is analysed. Results from the photo-ionisation models and their application to spectroscopic observations of HII regions are widely discussed in Paper II.

The number of ionising photons, $Q(H)$, and the H_α and H_β luminosities have been calculated in Paper I. The equivalent width of H_α and H_β are here calculated from the single population plus the nebular continuum (in the case of SSPs) or from the sum of all stellar populations plus nebular continuum, in the case of mixed populations (§4). From the computed SEDs, we previously calculated their corresponding total (stellar + nebular) uncontaminated colours in Paper I; now, using the CLOUDYs output, we compute the colours including the contamination from emission lines, as described in §2.3.

2.2 Basic Properties of HII Regions: Sizes and Luminosities

Throughout this work, we assume a scenario in which sufficient gas exists to be ionised (i.e., matter-bounded models have not been

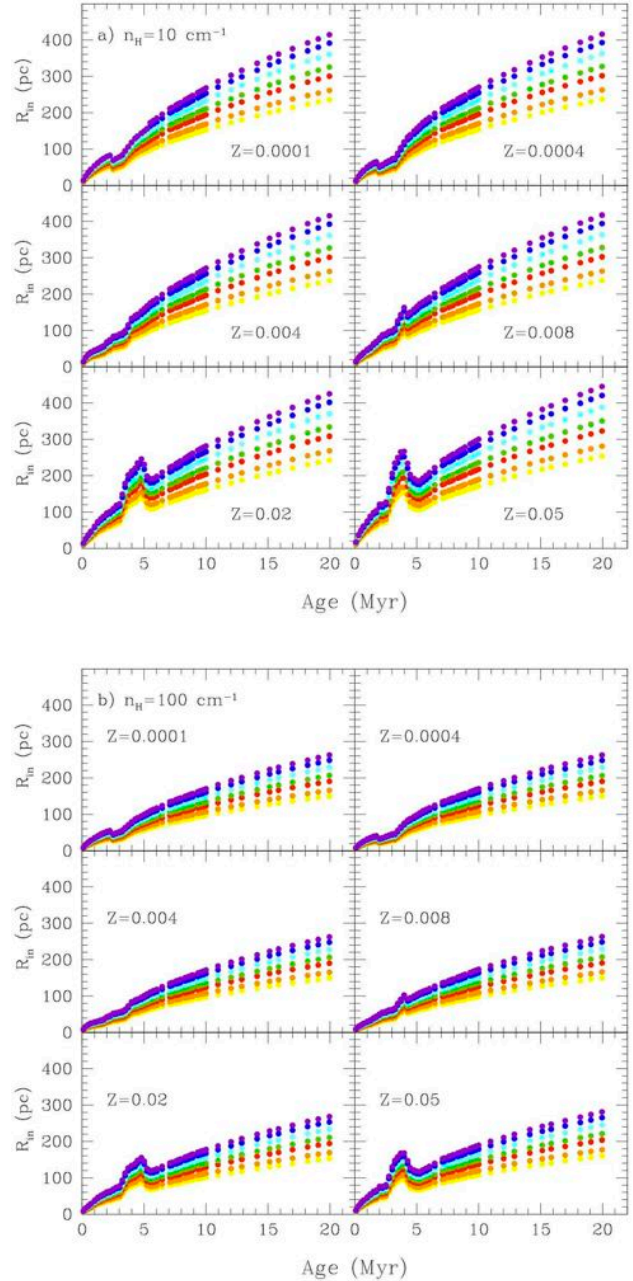


Figure 1. Region inner radius evolution: R_{in} (pc) vs cluster age (in Myr) for six different metallicities as labelled and different cluster mass, plotted in different colours. Cluster masses of 0.12 , 0.20 , 0.40 , 0.60 , 1.00 , 1.50 and $2.00 \times 10^5 M_\odot$ have been plotted in yellow, orange, red, green, cyan, blue and purple, respectively. The IMF is that of Salpeter with $m_{\text{low}} = 0.15 M_\odot$ and $m_{\text{up}} = 100 M_\odot$. Panel (a) shows models using a value of the gas electron density of $n_e = 10\text{ cm}^{-3}$, while in panel (b) they are computed with $n_e = 100\text{ cm}^{-3}$.

considered) and in which the birth of a star cluster, which we consider to be placed in the centre of a spherical region, is produced. In fact, we will not be able to detect the region in the visible until the neutral gas has started to be ionised, allowing detection of the emission lines (in particular the Balmer lines). For that, we need to have not only ionising photons but also certain nebula conditions, including a given gas density and an optical depth for the emitting

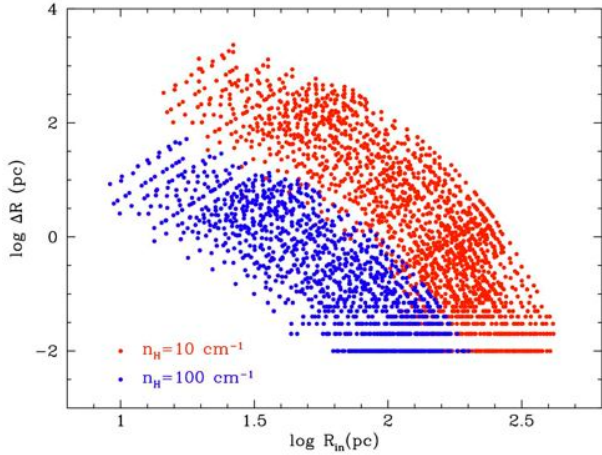


Figure 2. Shell thickness vs inner radius R_{in} (pc) for all metallicities, cluster masses and ages up to 20 Myr. Models with $n_e = 10 \text{ cm}^{-3}$ are plotted in red while models with $n_e = 100 \text{ cm}^{-3}$ are plotted in blue.

Table 1. Computed radii for the modelled stellar clusters of $Z = 0.008$ at selected ages for $n_e = 10 \text{ cm}^{-3}$. Complete table 1 for $n_e = 10$ and 100 cm^{-3} can be found online

Z	log τ (yr)	$n_e = 10 \text{ cm}^{-3}$			
		M_{cl} ($10^4 M_\odot$)	R_{in} (pc)	ΔR (pc)	R_{out} (pc)
0.008	6.30	1.2	45.440	1.72e+01	62.649
0.008	6.30	2.0	50.320	2.34e+01	73.717
0.008	6.30	4.0	57.810	3.55e+01	93.261
0.008	6.30	6.0	62.690	4.53e+01	108.005
0.008	6.30	10.0	69.440	6.16e+01	131.017
0.008	6.30	15.0	75.300	7.85e+01	153.832
0.008	6.30	20.0	79.760	9.33e+01	173.100
0.008	6.40	1.2	51.980	1.10e+01	62.994
0.008	6.40	2.0	57.570	1.50e+01	72.541
0.008	6.40	4.0	66.130	2.27e+01	88.873
0.008	6.40	6.0	71.720	2.90e+01	100.717
0.008	6.40	10.0	79.440	3.94e+01	118.846
0.008	6.40	15.0	86.150	5.02e+01	136.399
0.008	6.40	20.0	91.250	5.99e+01	151.115

region. These conditions occur around 0.5 - 1.0 Myr after cluster formation. As cluster evolves, the mechanical energy of the massive stars winds begins to sweep the gas away, compressing it and producing a shell. The wind-driven shell begins then to evolve with an initial phase of free expansion, followed by an adiabatic expansion phase, and then the swept-up material collapses to a thin, cold shell as a result of radiative cooling (Gibson, 1994; Tenorio-Tagle et al., 1999, e.g.).

At this stage the gas traps the ionisation front and the radiative phase begins. In this phase, the ionising photons are absorbed and the region cools via emission in the Balmer lines. In this process, the radius of the shock, limiting the inner border of the shell, R_{in} , evolves as (Castor et al., 1975):

$$R_{in} = 1.6(\epsilon/n)^{1/5} t^{3/5} \text{ (pc)}$$

where ϵ is the total injected mechanical energy per unit time in units of $10^{36} \text{ ergs s}^{-1}$, n is the interstellar medium density in units of cm^{-3} , and t is the age of the shell in units of 10^4 yr . We have used the radius computed by the above equation as given for each time t and $1 M_\odot$ in Table 4 from Paper I, scaled to the stellar cluster

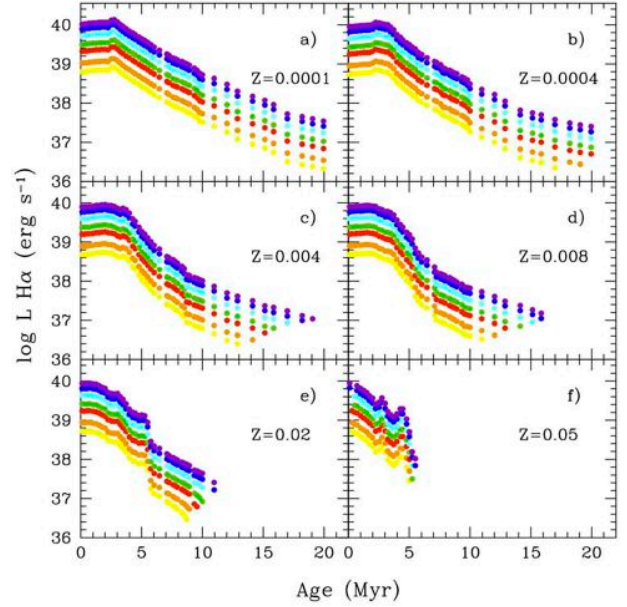


Figure 4. H_α evolution: $\log L H_\alpha$ (erg/s) vs cluster age (Myr) for six different metallicities and different cluster masses, plotted using the same colour coding that in Fig. 1.

mass of each model. We have extrapolated this bubble geometry to a shell structure formed by the combined effects of the mechanical energy deposition from the massive stars winds and SN explosions belonging to the ionising cluster. The ionised gas is assumed to be located in a thin spherical shell at that distance R_{in} from the ionising source (called R_s in Paper I). The shell inner radius results can be seen in Table 1.

The stacking of the material is caused by the shock wave providing a compression of the surrounding gas and therefore an increase of the recombinations ($\propto n^2$). Due to the balance between the ionising flux and the number of recombinations in the whole region, the presence of a shell more massive and larger will affect the overall size of the HII region and the ionisation front, which will be trapped inside the shell where all the photons will be employed. This happens when the following condition is fulfilled:

$$Q(H) = 4\pi R_{in}^2 \Delta R \beta_2 n_H^2 \quad (1)$$

where n_H is the density of the swept-up material and β_2 is the hydrogen recombination coefficient for levels higher than the fundamental one. Once the ionised front is trapped, the previously ionised material will recombine (corresponding to the initial swept-up mass (now in the shell and pushed by the shocked wind) which equates to the mass originally contained inside R_{in}).

We have therefore calculated the shell thickness, ΔR , and the outer radius, R_{out} (the sum of the inner radius plus the shell thickness). Table 1 partially shown here summarises the results for the modelled stellar clusters of $Z = 0.008$ at selected ages and $n_e = 10 \text{ cm}^{-3}$. The complete Table 1, available in electronic format, for all ages and metallicities, is computed for two values of the ionising gas electron density, since this parameter influences both the inner radius and the shell thickness: $n_e = 10 \text{ cm}^{-3}$ and $n_e = 100 \text{ cm}^{-3}$. In each one, columns are: the metallicity Z , the logarithm of the age, $\log \tau$ (in yr), the cluster mass, M_{cl} (in units of $10^4 M_\odot$), the HII region inner radius, R_{in} (in pc), the shell thickness, ΔR (in pc) and the total radius of the region, R_{out} (in pc), this latter radius being

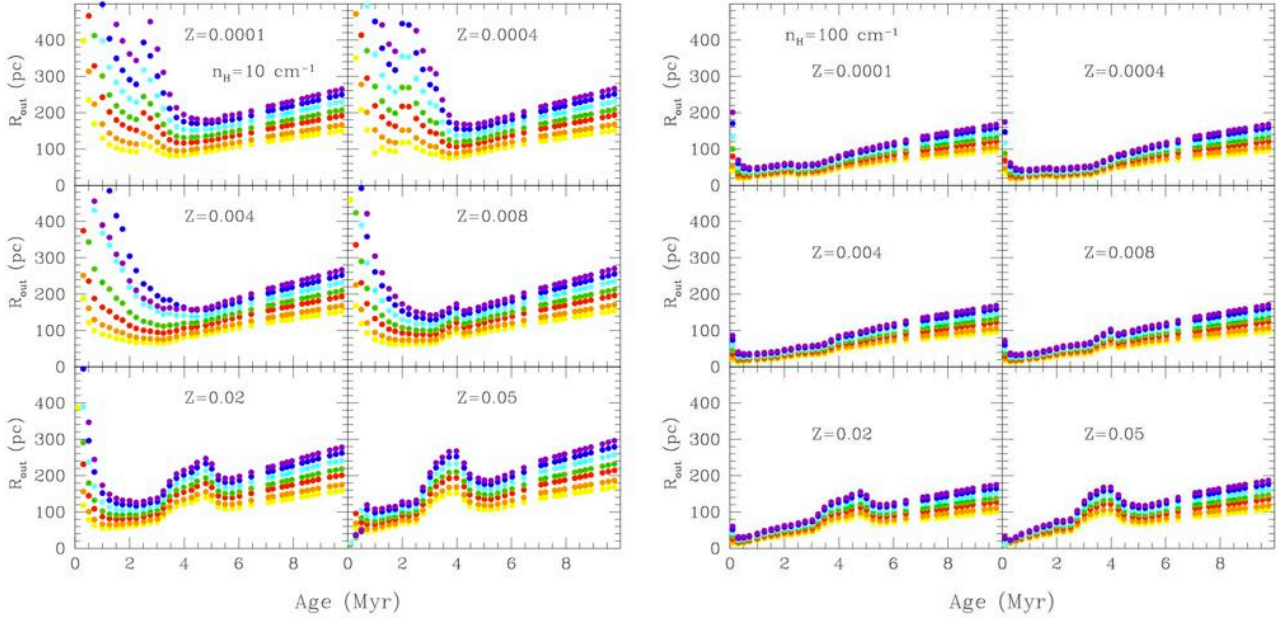


Figure 3. Region external radius evolution: R_{out} (pc) vs cluster age (Myr) for six different metallicities, all ages up to 20 Myr and different cluster’s mass, using the same colour coding that in Fig. 1

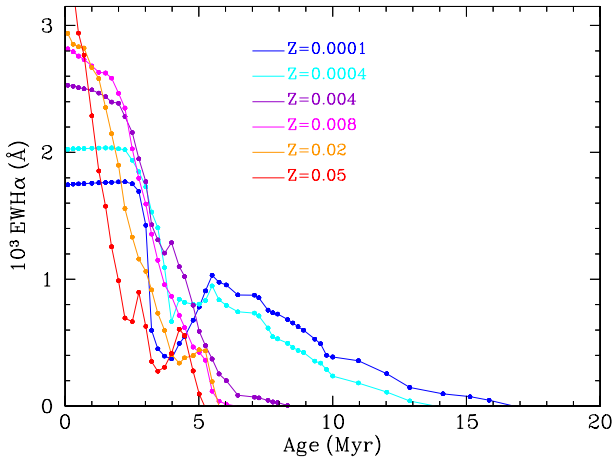


Figure 5. EW H_α evolution: EW H_α (Å) vs cluster age (Myr) for six different metallicities as labelled.

the most appropriate when comparing with real photometric radii observed in most HII regions (usually measured from H_α images). Both tables are available in electronic format.

The evolution of R_{in} is plotted in Fig. 1. At the beginning of the cluster’s evolution, the inner radius is small and the shell thickness is very large, as shown in Fig. 2, so that photons cannot escape. At a certain age (around 0.5 Myr) we start to detect the region by the emission line luminosity classifying it like a classical HII region. As the cluster evolves and its mechanical energy increases, the inner radius becomes larger while the shell becomes thinner. We will still see the region with a different emission line spectrum resulting from the cluster evolution (that changes both the ionising spectrum and the region geometry). We identify the observed object as an HII region (by definition) if we can detect hydrogen in emission, and this happens even after the emission line spectrum of

forbidden lines is over and up to 20 Myr (in average because there is a metallicity dependence).

The external radius of the region, which we would identify as the observed one in most photometric observations, is plotted against age in Fig. 3. In this figure we can see the differences compared to Fig. 1. This radius starts with a value of around hundreds of pc, smaller for $n_e = 100 \text{ cm}^{-3}$, and then decreases until SNe explosions begin to appear, which increase again the size of the region. Once the SNe explosions start to appear in the region, they can change the appearance and/or the geometry, however, we then should be more cautious when interpreting the observations based on our models, since the emission line spectrum will be the result of the shock and the photo-ionisation mechanisms. Our models do not include a shock contribution that can affect some emission lines, including [OII]6300 Å.

Besides the evolution of the radius of the region measured on the H_α images, we show in Fig. 4 and Fig. 5 the evolution of the intensity and equivalent width of H_α . In Fig. 4 we see that H_α luminosity maintains a high level for ages longer than 5 Myr and it maintains a detectable intensity until 20 Myr for the lowest abundances. This fact will have an impact on the colours, as we will see in the next section. The equivalent width shows a similar decreasing dependence with age, but also shows high values after the first 5.5 Myr for $Z=0.0001$ and $Z=0.0004$, while it falls to zero for the other abundances.

Fig 6 shows the outer radius of the region as a function of the logarithm of H_α luminosity. Models for different cluster masses are represented with different colours, as before. We see that HII regions may be quite large in size and luminosities for the lowest abundances compared with the metal-rich regions. Therefore if these regions are not observed, we need to consider potential observational selection effects. On the contrary, the metal-rich HII regions are much smaller, implying difficulty in observing these regions.

It seems that an inverse correlation between size and luminos-

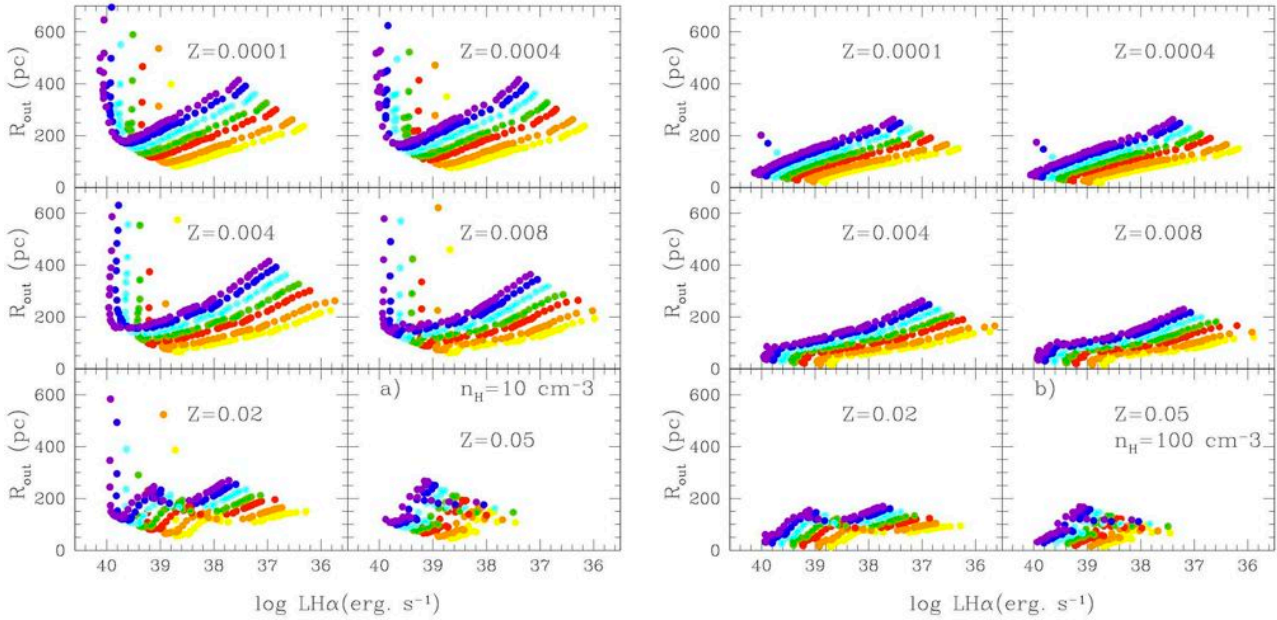


Figure 6. H_α evolution: R (pc) vs $\log(L H_\alpha)$ (erg s^{-1}) for six different metallicities and different cluster masses. Cluster masses have been plotted using the same colour coding that in Fig. 1. Panel (a) on the right shows models computed for a gas electron density of $n_e = 10 \text{ cm}^{-3}$, while panel (b) on the left uses a value of $n_e = 100 \text{ cm}^{-3}$.

ity arises from these plots for luminosities lower than $10^{40} \text{ erg s}^{-1}$ if the evolution of one cluster mass is followed, with larger radii for longer evolutionary times, when the H_α luminosity decreases. Observations instead show a positive correlation between size and luminosity. In fact our results are restricted due to the cluster masses selected in our computations. In Fig. 7a) we show as coloured points our results (with the same code than in Fig. 6) only for models with $\Delta R > 0.5 \text{ pc}$. This selection of models constrains the resulting luminosities to the range 10^{38} – $10^{40} \text{ erg s}^{-1}$. We compare these models with data from Mayya (1994); Ferreiro & Pastoriza (2004); Hakobyan et al. (2007) and Martínez-Delgado et al. (2009), shown as grey symbols. We see that some data fall out of the region defined by our models. In fact, observational points (which proceed from HII regions of different galaxies) show an abrupt decrease at a given luminosity, followed by a smooth increase that indicates the transition time in which massive star winds disappear and SNe start to increase the size of the bubble. However, some observational points seem to affect this change at an H_α luminosity higher than our models have. Thus, most observations from Ferreiro & Pastoriza (2004) show a behaviour that would be reproduced by models with a cluster mass larger than $2 \times 10^5 M_\odot$, our maximum cluster mass, or with a different IMF. Differences in the mass limits or slope of the IMF will change the mass distribution in the cluster generation, with direct consequences on the number of ionizing photons and LH_α . This effect was discussed in Paper I (Mollá et al. 2009). On the other end, many data from Mayya (1994) need a cluster mass smaller than $1.2 \times 10^4 M_\odot$, the lowest limit of the models computed here. These latter observations show a similarly strong increase around $LH_\alpha \sim 10^{38} \text{ erg s}^{-1}$, slightly smaller than that shown by the lowest cluster mass model. Therefore in panel b), we compare our models only with the other two sets of data from Hakobyan et al. (2007) and Martínez-Delgado et al. (2009) fitted by ionised clusters whose masses are within our model range. Doing so, we see that the observed correlation between size and luminos-

Table 2. Transmission value T of Johnson and SDSS filters. The complete table can be found in the online version.

λ (Å)	T
3050.	0.000
3100.	0.020
3150.	0.077
3200.	0.135
3250.	0.204
3300.	0.282
3350.	0.385
3400.	0.493

ity is reproduced with our models, the dispersion for is driven by the range in cluster masses. In that panel the red line is the least-squares straight fit to the data while the black line is the corresponding one for models. However, we warn that this correlation is not totally due to an evolutionary effect - as it has been argued in previous works - but a combination of the evolutionary state (age) and the mass of the cluster. A model with a given cluster mass shows a decrease in the size, while decreasing the H_α luminosity, before the SNe explosion time. Then, a new increase in the size of the region is seen (see Fig 6), while the H_α luminosity continues decreasing. Only when all cluster masses are included in the same plot (Fig. 7b) does the correlation between radius and luminosity arise clearly (e.g. Fig. 7b), showing, in the plane $\log R_{\text{out}} - \log LH_\alpha$, a slope similar to the observed one.

2.3 Colour Calculation

The filters included in this work are the optical broadband associated with Johnson's system (UBVRI) and the Sloan SDSS ugriz system. The transmission curves for both are shown in Fig. 8. Table

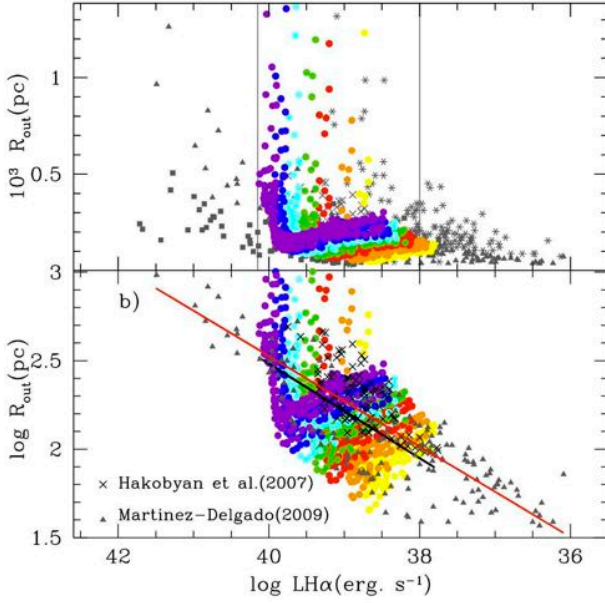


Figure 7. Relation of the outer radius R_{out} vs the H_α luminosity compared with observations. The coloured full dots are our models for $n_H = 10 \text{ cm}^{-1}$, selecting those with $\Delta R \geq 0.5 \text{ pc}$. In panel a) grey symbols represent the observational data from Mayya (1994); Ferreiro & Pastoriza (2004); Hakobyan et al. (2007); Martínez-Delgado et al. (2009) as asterisks, filled squares, crosses, and filled triangles, respectively. In panel b), with both axis in logarithmic scale, the (grey) triangles are data from Martínez-Delgado et al. (2009) and the (black) crosses are from Hakobyan et al. (2007). The red and black lines are the corresponding least-squares fit to the data set and models, respectively.

2, for which we show an example, and given in electronic format only, contains the transmission values as a function of wavelength for Johnson and SDSS filters.

The emission lines considered in this work are: 3727[OII], 3869[Ne III], 4101 H_β , 4340 H_γ , 4363[OIII], 4471 HeI, 4686 HeII, 4861 H_β , 4959[OIII], 5007[OIII], 5871 HeI, 6300[OI], 6312[SIII], 6548[NII], 6563 H_α , 6584[NII], 6716[SII], 6731[SII], 9069[SIII] and 9532[SIII]. The transmission of the selected broad band filters at these wavelengths is given in Table 3. Fig. 8 shows the filter transmission curves. Panel a) shows the UBVRI Johnson filters while panel b) shows the ugriz SDSS filters. We have marked in both panels the position of the 20 selected emission lines at $z=0$. We remind the reader that the use of these models is only valid for local, low-redshift, systems. For more distant objects, the shift of the lines has to be taken into account since the transmission of the filter at the wavelength of a given emission line (and therefore the contribution to the integrated colour) will also vary with redshift. We will discuss these effects in a future work.

The magnitudes have been calculated as:

$$m = -2.5 \log \int_{\lambda_1}^{\lambda_2} L_\lambda d\lambda + \sum_{i=1}^{20} T_i \times L_i + C \quad (2)$$

where λ_1 and λ_2 are the pass-band limits in each filter, L_λ is the stellar SED luminosity, L_i is the integrated luminosity in the narrow line for the line i and T_i the line filter transmission. In this calculation we assume that the line width is much narrower than the broad band filter pass-band. For Johnson's filters, C is the constant for flux calibration in the Vega system. According to the Girardi

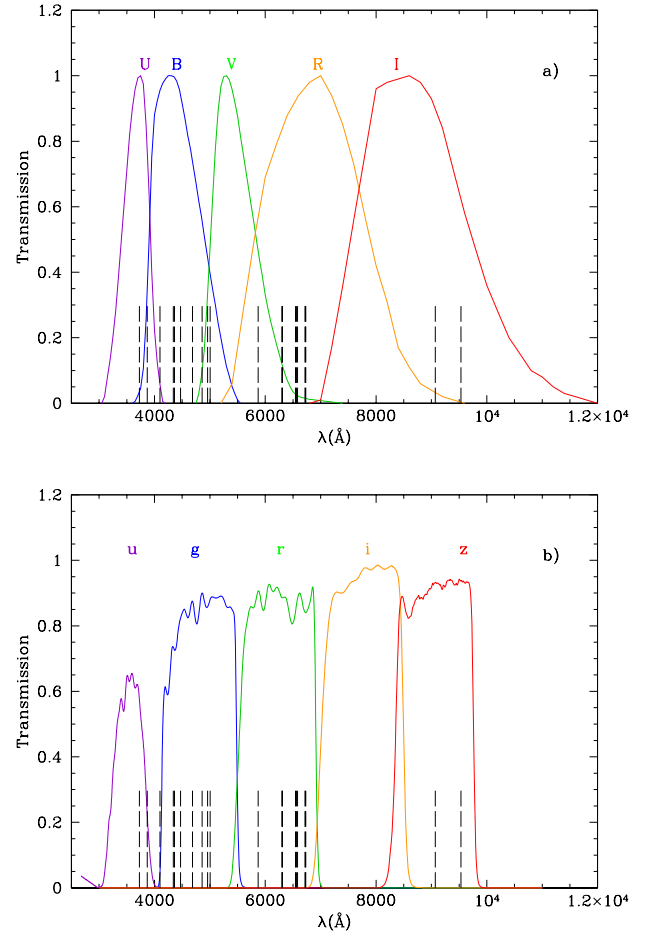


Figure 8. Transmission curves of a) U, B, V, R and I broad-band Johnson filters and b) u, g, r, i and z SDSS system filters. The figure also shows the location of the emission lines contributing to these filters.

et al. (2002) prescriptions, Vega has been taken as the average of Lejeune, Cuisinier & Buser (1997) models for $Z = 0.004$ and $Z = 0.008$ at $T = 9500\text{K}$ (Vega's data: $Z = 0.006$, $m_{bol} = 0.3319$, $BC = -0.25$ and $V=0.58$). C values are 2.19 (U), 3.29 (B when calculating U-B), 3.27 (B when calculating B-V), 2.54 (V), 2.76 (R) and 2.11 (I) when luminosities are in L_\odot units. In the SDSS system the constant is always -48.60. Details about calculation following Girardi et al. (2004) and Smith et al. (2002) can be seen in Paper I. Colours are the differences between the two selected magnitudes.

3 MODEL RESULTS FOR SSPS

3.1 Results

We have computed the colours from the pure continuum SSP SEDs (stellar + nebular), and the colours contaminated by the emission lines as described in §2.3. Model results for $Z = 0.008$ and some ages as an example are summarised in Table 4 and Table 5, for Johnson and SDSS colours, respectively. The complete tables are computed for two values of the ionising gas electron density, n_e , since this parameter leads to important differences in the emission line spectrum. This is well known and widely discussed in Paper II. Table 4 and Table 5 are computed for $n_e = 10 \text{ cm}^{-3}$ and for $n_e = 100 \text{ cm}^{-3}$. These tables provide the computed colours (in

Table 3. Transmission of the broad band filters at the rest wavelength of the selected emission lines

Emission line (Å)	T at U	T at B for U-B	T at B for B-V	T at V	T at R	T at I	T at u	T at g	T at r	T at i	T at z
3727[OII]	0.9966	0.0329	0.0438	0.0000	0.0000	0.0000	0.5781	0.0000	0.0000	0.0000	0.0000
3869[NeIII]	0.7837	0.3321	0.3911	0.0000	0.0000	0.0000	0.2263	0.0000	0.0000	0.0000	0.0000
4101 H δ	0.0557	0.9556	0.9962	0.0000	0.0000	0.0000	0.0009	0.0493	0.0000	0.0000	0.0000
4340 H γ	0.0000	0.9983	0.9612	0.0000	0.0000	0.0000	0.0005	0.7353	0.0000	0.0000	0.0000
4363[OIII]	0.0000	0.9947	0.9507	0.0000	0.0000	0.0000	0.0000	0.7253	0.0000	0.0000	0.0000
4471 HeI	0.0000	0.9405	0.8768	0.0000	0.0000	0.0000	0.0000	0.8237	0.0000	0.0000	0.0000
4686 HeII	0.0000	0.7372	0.6621	0.0000	0.0000	0.0000	0.0000	0.8748	0.0000	0.0000	0.0000
4861 H β	0.0000	0.5556	0.4859	0.0943	0.0000	0.0000	0.0000	0.9004	0.0000	0.0000	0.0000
4959[OIII]	0.0000	0.4474	0.3873	0.3265	0.0000	0.0000	0.0000	0.8577	0.0000	0.0000	0.0000
5007[OIII]	0.0000	0.3934	0.3380	0.4829	0.0000	0.0000	0.0000	0.8820	0.0000	0.0000	0.0000
5871 HeI	0.0000	0.0000	0.0000	0.4638	0.5828	0.0000	0.0000	0.0000	0.9063	0.0000	0.0000
6300[OI]	0.0000	0.0000	0.0000	0.1200	0.8394	0.0000	0.0000	0.0000	0.8861	0.0000	0.0000
6312[SIII]	0.0000	0.0000	0.0000	0.1134	0.8447	0.0000	0.0000	0.0000	0.8855	0.0000	0.0000
6548[NII]	0.0000	0.0000	0.0000	0.0273	0.9263	0.0000	0.0000	0.0000	0.8456	0.0000	0.0000
6563 H α	0.0000	0.0000	0.0000	0.0250	0.9304	0.0000	0.0000	0.0000	0.8625	0.0000	0.0000
6584[NII]	0.0000	0.0000	0.0000	0.0225	0.9359	0.0000	0.0000	0.0000	0.8842	0.0000	0.0000
6716[SII]	0.0000	0.0000	0.0000	0.0154	0.9622	0.0000	0.0000	0.0000	0.8417	0.0001	0.0000
6731[SII]	0.0000	0.0000	0.0000	0.0148	0.9654	0.0000	0.0000	0.0000	0.8404	0.0002	0.0000
9069[SIII]	0.0000	0.0000	0.0000	0.0000	0.0314	0.9060	0.0000	0.0000	0.0000	0.0003	0.9326
9532[SIII]	0.0000	0.0000	0.0000	0.0000	0.0000	0.6210	0.0000	0.0000	0.0000	0.0003	0.9381

Johnson and SDSS systems respectively) together with other cluster parameters that can be obtained from photometrical observations. Table 4 columns are: the metallicity Z , the logarithm of the age τ (in yr), the cluster mass M_{cl} (in M_{\odot}), the logarithm of the H_{β} and H_{α} luminosities, $L_{H_{\beta}}$ and $L_{H_{\alpha}}$ (both in erg.s^{-1}), the absolute magnitude V and colours $(U-B)_c$, $(B-V)_c$, $(V-R)_c$ and $(R-I)_c$ contaminated with the emission lines, the uncontaminated absolute magnitude V , and colours $U-B$, $B-V$, $V-R$ and $R-I$, (which obviously do not change with the mass of the stellar cluster). Table 5 columns are: the metallicity Z , the logarithm of the age τ (in yr), the cluster mass M_{cl} (in M_{\odot}), the equivalent widths of H_{β} and H_{α} , $EW(H_{\beta})$ and $EW(H_{\alpha})$ in Å, the absolute magnitude g and colours $(u-g)_c$, $(g-r)_c$, $(r-i)_c$ and $(i-z)_c$ contaminated with the emission lines, the uncontaminated absolute magnitude g and colours $u-g$, $g-r$, $r-i$ and $i-z$. The whole table with results for all ages and metallicities will be given in electronic format.

3.2 Colour Evolution

Fig 9 shows the results of the Johnson colours' evolution with and without the emission line contribution for instantaneous young bursts (SSPs) between 1 and 20 Myr in age. We show four colours as a function of the cluster age (in Myr): $U-B$ (left columns); $B-V$ (left-middle columns); $V-R$ (right-middle columns) and $R-I$ (right columns). A different metallicity ($Z = 0.0001, 0.0004, 0.004, 0.008, 0.02$, and 0.05) is displayed from top to bottom, as labelled in the $U-B$ diagram of each row.

Colours from the clusters without the emission line contamination are plotted with a solid black line. Colours including the contribution of the emission line spectrum are plotted with different colours, according to cluster mass - 0.12, 0.20, 0.40, 0.60, 1.00, 1.50 and $2.00 \times 10^5 M_{\odot}$, from the lighter colour (yellow) to the darkest one (purple), using the same coding as in the previous figures. As explained before, a different cluster mass implies not only a variation in the number of ionising photons but also a change in the size of the associated HII region due to the assumption (in our

models) that the bubble radius depends on the total mechanical energy deposited by the cluster's winds and supernovae.

This figure shows that colours have very different values when the emission line contribution is included in the calculation. These variations in the expected colours for a young stellar cluster are especially important for low-to-intermediate metallicities ($Z = 0.0004$ to 0.008); this seems reasonable, as the emission lines in the visible have the strongest intensities in this abundance range.

The contaminated colours $U-B$ and $B-V$ for all metallicities, and all colours for high-metallicity ($Z > 0.008$) evolve with age, reaching the uncontaminated colours as soon as the emission lines disappear near 5.5 Myr (this value depends on the metallicity, as discussed in Paper II). However, $V-R$ and $R-I$ contaminated colours at low metallicity still show variations with respect to the uncontaminated colours even up to ages of ~ 20 Myr.

This is because these colours are contaminated by hydrogen emission lines, and the R -band is the most highly contaminated. This indicates the presence of ionising photons - i.e., a young population - which produces H_{α} emission that falls almost in the centre of the R -band, near to the maximum of the filter transmission curve, producing a redder $V-R$ colour simultaneous to a bluer $R-I$.

We note again that H_{α} emission is expected even for ages beyond 5.5 Myr (when other emission lines cannot be produced) and is detectable up until ages of 10 to 20 Myr, depending upon metallicity. Up to now, arguments for a reddened colour had been based upon the claim for an old underlying population or a dust excess. We show here that a reddened $V-R$ colour, with a contemporaneous blue $R-I$, in a SSP, can be explained in a new way: with the presence of a young population, which possesses sufficient numbers of ionising photons to produce H_{α} emission.

In a similar manner, Fig. 10 shows the effect of these emission lines in the SDSS filter system. Differences in colours, with and without the contribution of the emission lines, are even more substantial than in the Johnson system, reaching in some colours, difference of up to one magnitude.

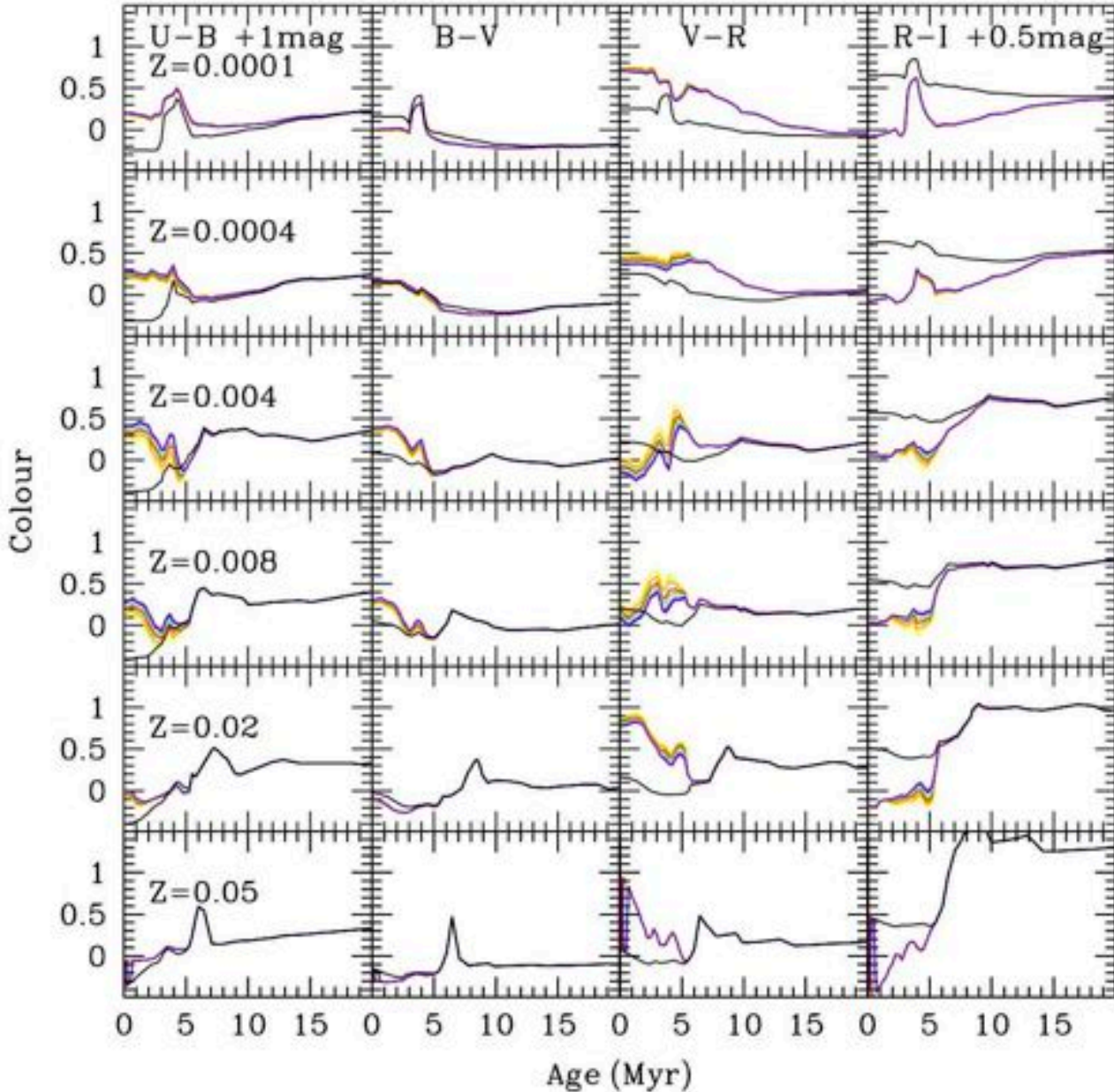


Figure 9. Photometric evolution of colours U-B, B-V, V-R and R-I vs cluster age (in Myr) for $Z = 0.0001, 0.0004, 0.004, 0.008, 0.02$ and 0.05 from top to bottom panels as labelled. Each colour corresponds to a different cluster mass as in previous figures.

3.3 Colour-Colour Diagrams

Fig 11 shows four Johnson colour-colour diagrams for SSPs up to 20 Myr in age: U-B vs B-V (top left); B-V vs V-R (top right); B-V vs V-I (bottom left) and V-R vs R-I (bottom right). We show results for $Z = 0.008$, panel d) and the corresponding ones to other metallicities, Fig.11a, 11b, 11c, 11e and 11f will be in electronic format. Different colours correspond to different cluster masses, as in Fig 9. Black open ones correspond to the youngest ages including the nebular continuum contribution but not the emission lines.

In panels of the U-B vs B-V diagram we observe that when young stellar populations (contaminated and uncontami-

nated) colours are plotted, the points fall out of the location expected when standard SSP synthetic colours without the emission line (or continuum) contribution are used. The nebular continuum moves the points out of the standard sequence for old (age ≥ 20 Myr, see Fig. 13) stellar populations. Moreover, when the emission lines contribution is included in the colour calculation, the sequence shows almost the original slope, but moved to an almost parallel line for $Z < 0.02$, with higher B-V for similar U-B.

Observing the B-V vs V-R diagram, the situation changes, since the contaminated colours fall in the same region of the plot, albeit in an orthogonal sense, in most cases. This behaviour appears

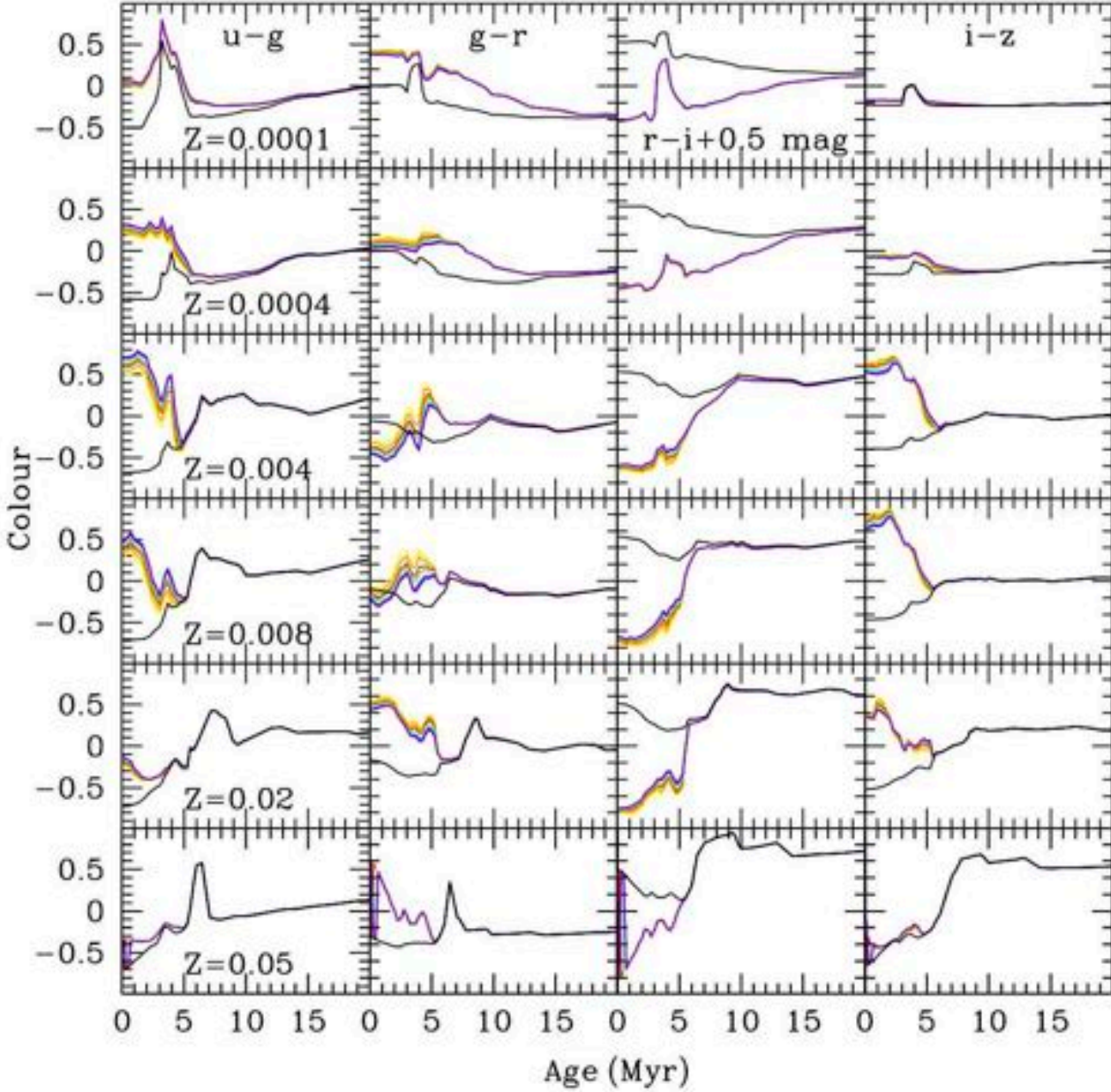


Figure 10. Photometric evolution of colours $u-g$, $g-r$, $r-i$ and $i-z$ vs cluster age (in Myr) for $Z = 0.0001, 0.0004, 0.004, 0.008, 0.02$ and 0.05 from top to bottom panels as labelled. Each colour corresponds to a different cluster mass as in previous figures.

independent of the stellar cluster mass, especially for $Z = 0.004$ and $Z = 0.008$. This characteristic might allow one to predict the strength of a new starburst overlaid upon an underlying and older stellar population. Further, one might determine the age of this burst from the distance of a given point to the canonical line of old ages. This effect is stronger when mixed population models (§4) are interpreted.

In the $B-V$ vs $V-I$ diagrams, the youngest stellar populations show colours with the same trend as the uncontaminated ones for some metallicity cases, while appearing orthogonal for others. On the one hand, the H_α emission reddens the $V-I$ colour. On other, if

the metallicity is intermediate ($Z=0.004-0.008$), the oxygen emission lines also increase the luminosity in the V -band, since the nebular cooling is mostly done through $[OIII]$ lines. The resulting populated area is very different from the one with uncontaminated SSP colours.

Finally, the $V-R$ vs $R-I$ diagram is the one most affected by the contribution of H_α emission to the R -band luminosity (which dominates over the effect of sulphur lines contributing to the I -band). This diagram may therefore be useful to check if these contamination effects (due to a young ionising population) is present regardless of the cluster physical properties, since all the metallicities and

Table 4. Johnson colours evolution results for the modelled stellar clusters of $Z = 0.008$ at some selected ages for $n_e = 10 \text{ cm}^{-3}$. Complete table 4 for all ages and metallicities and for $n_e = 10$ and 100 cm^{-3} can be found in the online version

$n_e = 10 \text{ cm}^{-3}$														
Z	$\log \tau$ (yr)	M_{cl} (M_{\odot})	LH β (erg s^{-1})	LH α (erg s^{-1})	V_c	(U-B) $_c$	(B-V) $_c$	(V-R) $_c$	(R-I) $_c$	V	U-B	B-V	V-R	R-I
0.008	6.30	$1.2 \cdot 10^4$	38.23	38.70	-10.407	-1.123	0.130	0.431	-0.437	-9.648	-1.356	-0.015	0.159	0.019
0.008	6.30	$2 \cdot 10^4$	38.45	38.92	-10.998	-1.060	0.151	0.365	-0.413	-10.203	-1.356	-0.015	0.159	0.019
0.008	6.30	$4 \cdot 10^4$	38.75	39.22	-11.793	-0.984	0.174	0.290	-0.391	-10.955	-1.356	-0.015	0.159	0.019
0.008	6.30	$6 \cdot 10^4$	38.93	39.40	-12.256	-0.944	0.186	0.253	-0.384	-11.395	-1.356	-0.015	0.159	0.019
0.008	6.30	$1 \cdot 10^5$	39.15	39.62	-12.835	-0.899	0.199	0.212	-0.378	-11.950	-1.356	-0.015	0.159	0.019
0.008	6.30	$1.5 \cdot 10^5$	39.33	39.80	-13.293	-0.869	0.208	0.183	-0.377	-12.390	-1.356	-0.015	0.159	0.019
0.008	6.30	$2 \cdot 10^5$	39.45	39.92	-13.618	-0.848	0.215	0.163	-0.378	-12.703	-1.356	-0.015	0.159	0.019
0.008	6.40	$1.2 \cdot 10^4$	38.15	38.62	-10.166	-1.243	-0.028	0.608	-0.493	-9.715	-1.288	-0.075	0.104	-0.012
0.008	6.40	$2 \cdot 10^4$	38.37	38.84	-10.753	-1.191	-0.009	0.540	-0.459	-10.270	-1.288	-0.075	0.104	-0.012
0.008	6.40	$4 \cdot 10^4$	38.67	39.15	-11.545	-1.124	0.015	0.462	-0.427	-11.022	-1.288	-0.075	0.104	-0.012
0.008	6.40	$6 \cdot 10^4$	38.85	39.32	-12.005	-1.088	0.028	0.423	-0.413	-11.462	-1.288	-0.075	0.104	-0.012
0.008	6.40	$1 \cdot 10^5$	39.07	39.55	-12.582	-1.047	0.041	0.381	-0.400	-12.017	-1.288	-0.075	0.104	-0.012
0.008	6.40	$1.5 \cdot 10^5$	39.25	39.72	-13.038	-1.018	0.051	0.351	-0.392	-12.457	-1.288	-0.075	0.104	-0.012
0.008	6.40	$2 \cdot 10^5$	39.37	39.85	-13.362	-0.998	0.057	0.332	-0.389	-12.770	-1.288	-0.075	0.104	-0.012

Table 5. SDSS colour evolution results for the modelled SSP of $Z = 0.008$ at some selected ages for all ages and metallicities and for $n_e = 10 \text{ cm}^{-3}$. Complete table 5, for $n_e = 10$ and 100 cm^{-3} can be found in the online version

$n_e = 10 \text{ cm}^{-3}$														
Z	$\log \tau$ (yr)	M_{cl} (M_{\odot})	EW $H\beta$ (\AA)	EW $H\alpha$ (\AA)	g_c	(u-g) $_c$	(g-r) $_c$	(r-i) $_c$	(i-z) $_c$	g	u-g	g-r	r-i	i-z
0.008	6.30	$1.2 \cdot 10^4$	409.97	2466.30	-10.249	-0.020	0.136	-1.278	0.863	-9.280	-0.678	-0.154	-0.019	-0.445
0.008	6.30	$2 \cdot 10^4$	409.97	2466.30	-10.840	0.053	0.067	-1.245	0.852	-9.835	-0.678	-0.154	-0.019	-0.445
0.008	6.30	$4 \cdot 10^4$	409.97	2466.30	-11.634	0.139	-0.011	-1.208	0.833	-10.587	-0.678	-0.154	-0.019	-0.445
0.008	6.30	$6 \cdot 10^4$	409.97	2466.30	-12.098	0.186	-0.051	-1.192	0.822	-11.027	-0.678	-0.154	-0.019	-0.445
0.008	6.30	$1 \cdot 10^5$	409.97	2466.30	-12.677	0.236	-0.094	-1.174	0.803	-11.582	-0.678	-0.154	-0.019	-0.445
0.008	6.30	$1.5 \cdot 10^5$	409.97	2466.30	-13.134	0.270	-0.124	-1.160	0.784	-12.022	-0.678	-0.154	-0.019	-0.445
0.008	6.30	$2 \cdot 10^5$	409.97	2466.30	-13.459	0.294	-0.144	-1.153	0.771	-12.335	-0.678	-0.154	-0.019	-0.445
0.008	6.40	$1.2 \cdot 10^4$	314.46	2027.40	-10.006	-0.287	0.314	-1.238	0.697	-9.382	-0.617	-0.218	-0.082	-0.420
0.008	6.40	$2 \cdot 10^4$	314.46	2027.40	-10.594	-0.222	0.241	-1.198	0.693	-9.937	-0.617	-0.218	-0.082	-0.420
0.008	6.40	$4 \cdot 10^4$	314.46	2027.40	-11.387	-0.142	0.158	-1.155	0.682	-10.689	-0.617	-0.218	-0.082	-0.420
0.008	6.40	$6 \cdot 10^4$	314.46	2027.40	-11.846	-0.101	0.118	-1.134	0.672	-11.129	-0.617	-0.218	-0.082	-0.420
0.008	6.40	$1 \cdot 10^5$	314.46	2027.40	-12.423	-0.054	0.073	-1.112	0.660	-11.684	-0.617	-0.218	-0.082	-0.420
0.008	6.40	$1.5 \cdot 10^5$	314.46	2027.40	-12.879	-0.020	0.041	-1.095	0.648	-12.124	-0.617	-0.218	-0.082	-0.420
0.008	6.40	$2 \cdot 10^5$	314.46	2027.40	-13.204	0.004	0.021	-1.088	0.641	-12.437	-0.617	-0.218	-0.082	-0.420

cluster mass change the colour-colour diagram with respect to the canonical uncontaminated models. Fig. 12 is similar to Fig 11 for SDSS colour-colour diagrams.

In summary, our remarkable conclusions from Fig 11 and Fig. 12 are: 1) The youngest stellar population models - therefore, those contaminated most by emission lines - do not follow the generic trend shown by SSP colours calculated in the absence of this emission line contribution, and 2) these young regions' colours fall in a well-defined region for each colour-colour diagnostic diagram. In some cases (e.g. B-V vs V-R), this region of contaminated colours is located orthogonally to the region where the canonical uncontaminated colours reside. It is clear that emission lines change strongly the location of the models in any given colour-colour diagram. We emphasise that most observers use canonical (uncontaminated and probably without the nebular continuum contribution) models to compare with their star-forming region photometry and use these to derive the properties of the unveiled young stellar population. In some cases, a reddened colour is often interpreted as implying the existence of an old population. As we have demonstrated in the previous paragraphs and shown in the accompanying figures, we can interpret reddening in some colours,

instead, actually as a proof of the existence of a young population. In other cases the lack of good fitting between the classical photometrical models (uncontaminated colours) and the observations is interpreted as extinction (reddened colours are interpreted as dust contamination). This can lead to an overestimation of dust and extinction when this value is derived from photometric data in HII regions, even after correcting for an underlying old component. In summary, the interpretation has to be done using contaminated models and of course the impact will depend on the colours chosen.

Finally, and as an extension of Fig. 11 and Fig. 12, we have used all the models together in Fig. 13. This figure shows the eight different colour-colour diagrams (4 for Johnson and 4 for SDSS filters). Models from different metallicities have been plotted together. Large black symbols correspond to the young stellar cluster colours without contamination of emission line spectra. Coloured symbols correspond to values that include the emission line contribution for the youngest ages (between 1.0 and 5.0 Myr). Different cluster masses (which, we remind, in our models implies different HII regions' inner radii and therefore different emission line spectrum), have been represented with the same colours as seen previously in Fig 9 and Fig 10. Finally, together with the young clus-

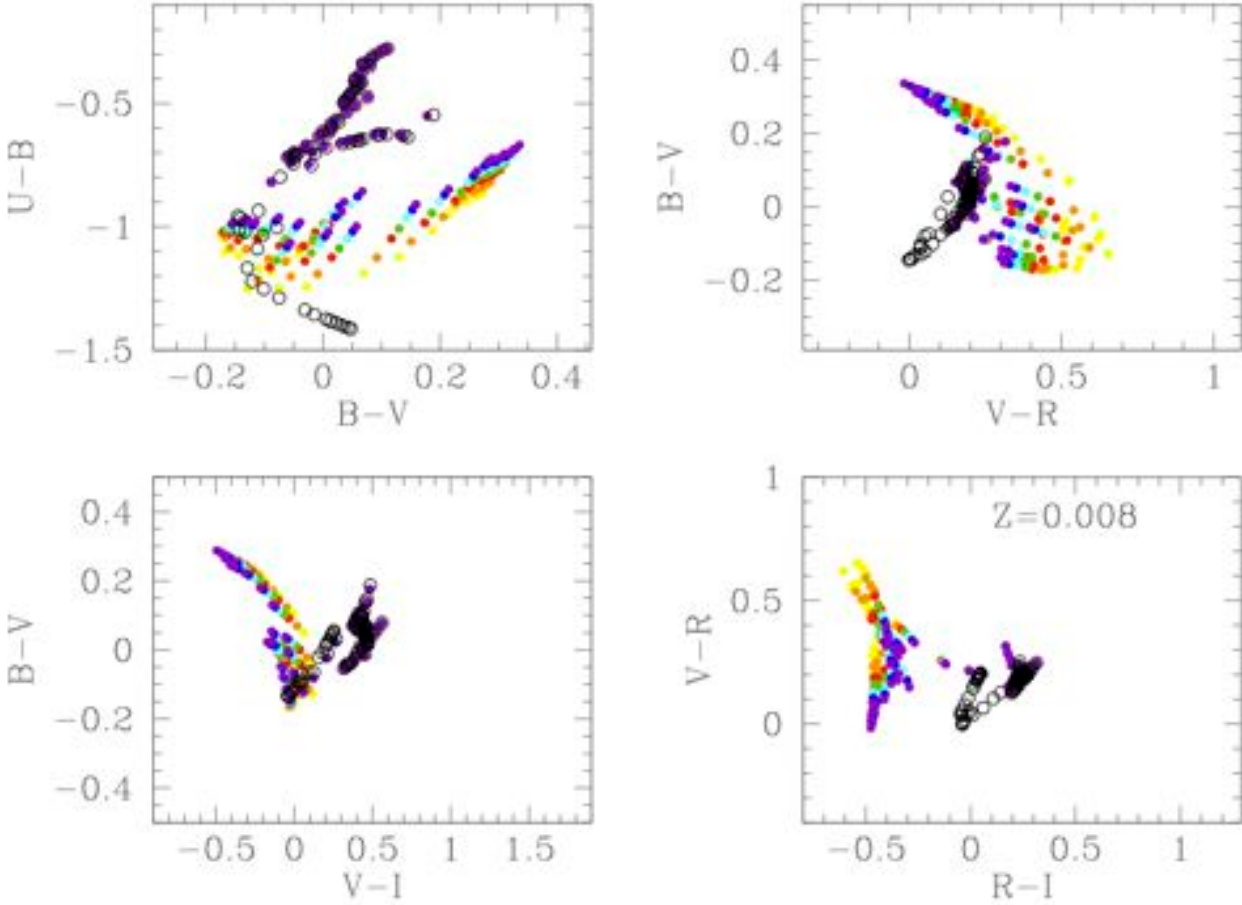


Figure 11. Colour-Colour diagrams for young clusters. Panel d) Results for $Z=0.008$: top-left) $U-B$ vs $B-V$; top-right) $B-V$ vs $V-R$; bottom-left) $B-V$ vs $V-I$ and right-bottom) $V-R$ vs $R-I$. Open and full dots are the results without and with emission lines. Each colour corresponds to a different cluster mass. The same figures for the other metallicities: $Z = 0.0001, 0.0004, 0.004, 0.02$ and 0.05 , panels a), b), c), e) and f) are given in electronic format.

ters, we have included the whole evolutionary sequence, that is all metallicities in the range $Z = 0.0001 - 0.05$ and all ages from 20 Myr up to 15 Gyr, obtained with PopSTAR in Paper I, as grey full dots. This figure shows a clear age sequence for SSP ages older than 10 Myr in all colour-colour diagrams. This sequence places pure young populations (ages below 10-20 Myr) and pure old SSPs in completely different areas in the plot since the youngest fall out of the old sequence. We have plotted a dashed line in each colour-colour diagram to separate the zone where young stellar clusters would reside from the one where the old stellar populations fall. When the young populations with the contaminated colours are included, the diagrams change again since some colours are redder, more similar to the ones of older populations, but others are bluer, and therefore points are located in different diagram regions. The problem is even worse when mixed populations are studied as discussed in §4.

3.4 Colours vs Other Photometric Parameters

We have used in this work not only the information coming from the colours, but also that associated with other photometric parameters. Fig 14 shows the relationship between colours (both John-

son and SDSS) and equivalent widths of H_α . We have plotted all masses, metallicities and ages together in the same plot.

The original colours without the emission line contribution are the full green dots. These models define a clear sequence in all plots. Colours including the contribution of emission lines are the black crosses. The equivalent width in this case does not change with the emission lines, while the colours do. This causes the points to move up or down with respect to their original position. Panel a) shows that in a given time, $U-B$ becomes redder and the points move up slightly. This occurs when $EW(H_\alpha)$ is still quite high (young ages).

The same occurs in panel c) with $V-R$, although in this case the reddening extends also for low values of $EW(H_\alpha)$. Changes in panel b), the $B-V$ colour, are less evident because emission lines contaminate both B- and V-band in a comparable proportion. Panel d) shows how the $R-I$ points move down (towards bluer colours), since R is a highly contaminated band. We cannot find a clear metallicity dependence in these plots.

The figure of $EW H_\alpha$ vs $U-B$ is particularly interesting because most of the data cannot be reproduced with pure single stellar populations as Martín-Manjón et al. (2008, and references therein) showed. The usual explanation was the existence of an underlying

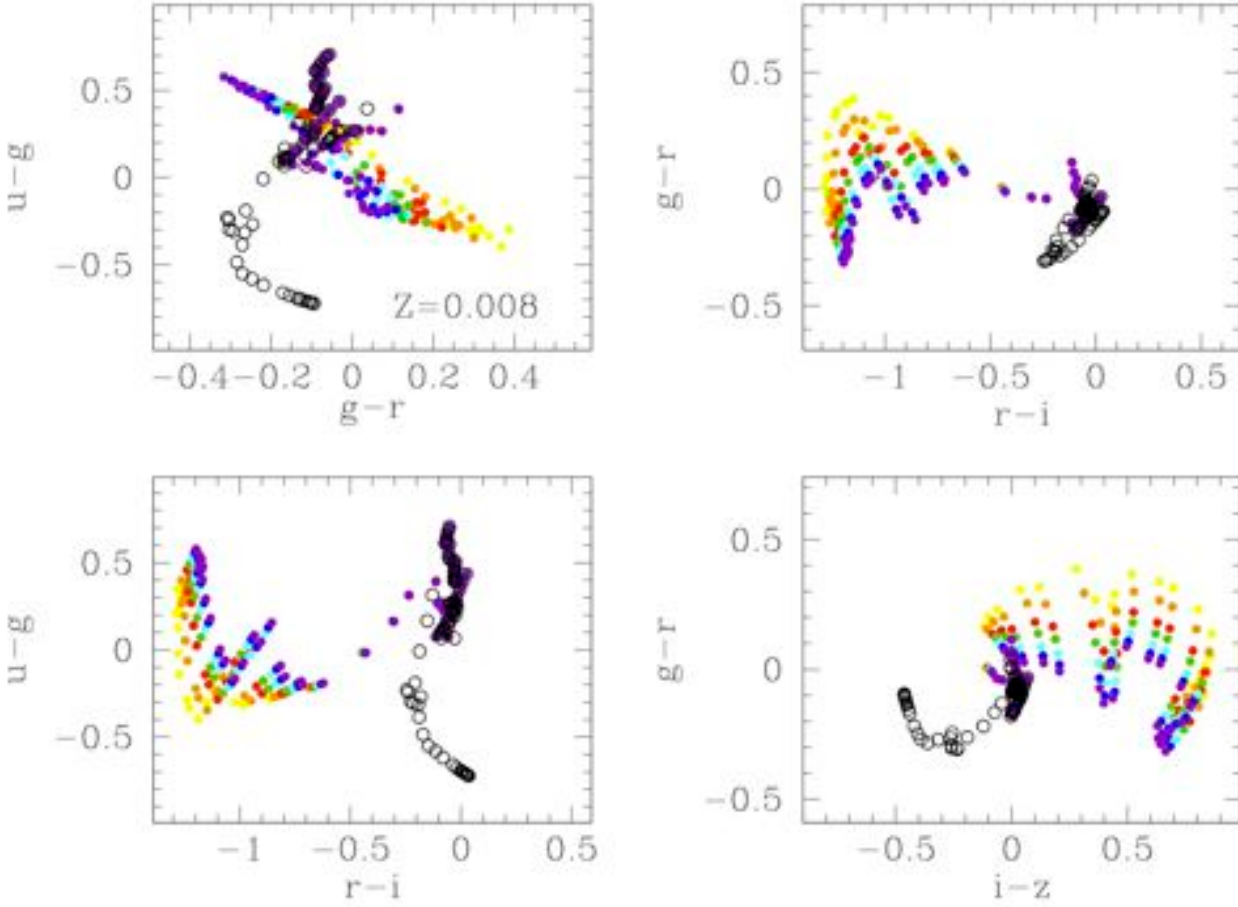


Figure 12. Colour-Colour diagrams for young clusters. Panel d) Results for $Z=0.008$: top-left) $u-g$ vs $g-r$; top-right) $g-r$ vs $r-i$; bottom-left) $u-g$ vs $r-i$ and bottom-right) $r-i$ vs $i-z$. R Open and full dots are the results without and with emission lines. Each colour corresponds to a different cluster mass . The same figures for the other metallicities: $Z = 0.0001, 0.0004, 0.004, 0.02$ and 0.05 , panels a), b), c), e) and f) are given in electronic format.

older stellar population which, in addition to the recent starburst, could reproduce simultaneously a red U-B color together with the observed values of the Balmer lines equivalent widths. We claim that, even without adding an old population, an U-B reddening due to the strong contribution of the emission lines in this color is predicted. The effect is a larger dispersion in the plot, erasing the original trend in the plot U-B color vs $EW(H_\alpha)$ which showed an age sequence from the high equivalent width and blue colour to the low equivalent width and red colour.

Panels e) to h) represent the same kind of plots but for the SDSS colours. A clear separation of the colour sequences without and with emission lines is seen, mainly for the $r-i$ colour, where H_α has a stronger contribution. These plots may be useful to separate young (ages $\tau < 20$ Myr and clear H_α emission) from old stellar populations.

4 MIXED POPULATIONS

All the models presented in the previous sections assume that there is a single cluster producing the colours of the observed region. In more massive objects where different stellar populations coexist, the contribution of the youngest cluster (responsible for the ion-

isation and the emission lines) mass to the total stellar mass can change the final broadband magnitudes and therefore the colours. The more massive the young population, the more important the contribution of emission lines to the integrated colours. On the contrary, objects where the young population contribution is small can be well-fit by canonical synthetic colours since the contribution of the emission lines to the total luminosity and therefore to the colours will be minimal.

The calculation of the mixed population (combination of young and old clusters) colours requires a good reference grid of models that allows one to derive the physical properties of composite stellar systems when only photometric information is available. This section is devoted to these composite models in which we have a young ionising stellar burst superimposed upon an underlying old population. The difference with earlier work in the field (see Paper I for a review of Evolutionary Synthesis Models) is that the emission lines coming from the ionisation and the nebular continuum, produced both by the young cluster, are included when computing the integrated colours. We remark the fact that these models have been computed in a consistent manner by taking into account the cluster evolution (and therefore the mechanical energy) to derive the region's photometric size and therefore the radius that, together

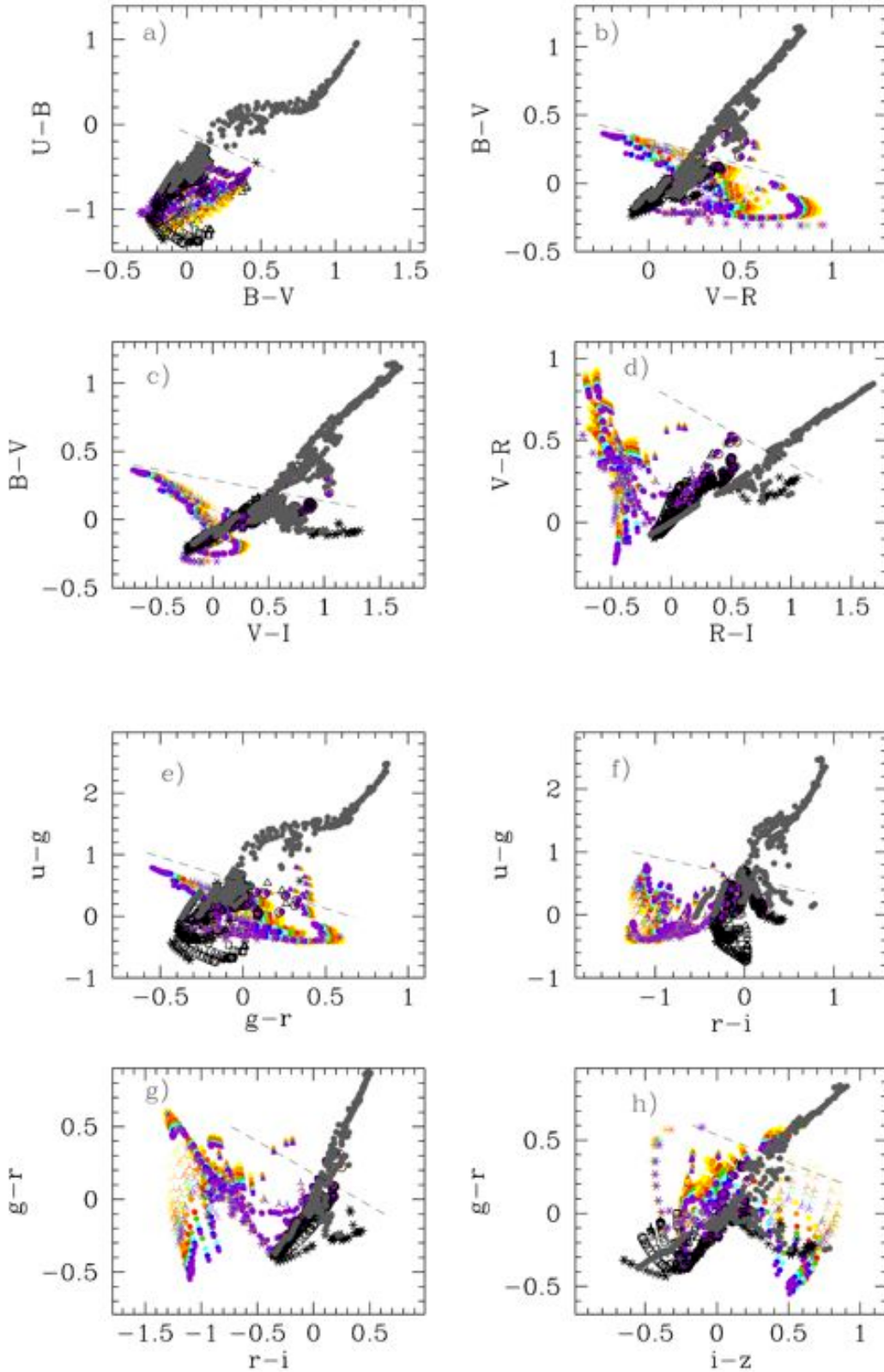


Figure 13. Colour-colour diagrams evolution for all ages and all metallicities. Panels show a) $U-B$ vs $B-V$; b) $B-V$ vs $V-R$; c) $B-V$ vs $V-I$, d) $V-R$ vs $R-I$, e) $u-g$ vs $g-r$; f) $u-g$ vs $r-i$; g) $g-r$ vs $r-i$ and h) $g-r$ vs $i-z$. Dashed black lines separate the old stellar population region ($\tau > 20$ Myr) from the zone of young ones. Colours represent different cluster masses, as in previous figures. Grey full dots correspond to the stellar population colours without any nebular contribution. The black symbols represent colours including the nebular continuum contribution but not the emission lines one. All cluster metallicities and ages have been included in the figure.

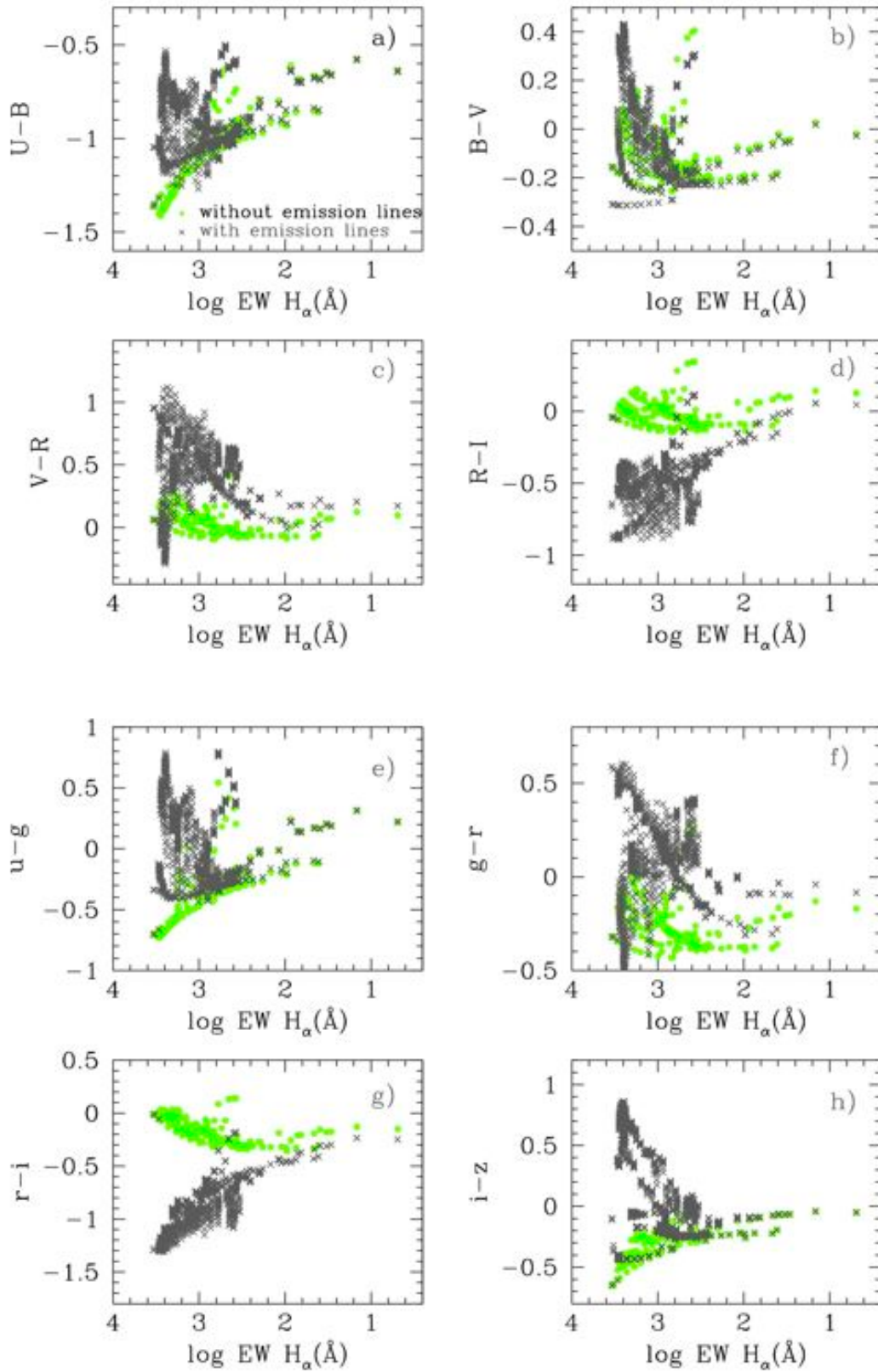


Figure 14. Colours vs log of $H\alpha$ equivalent width diagrams: a) $U-B$ vs $\log EW(H\alpha)$; b) $B-V$ vs $\log EW(H\alpha)$; c) $V-R$ vs $\log EW(H\alpha)$; d) $R-I$ vs $\log EW(H\alpha)$; e) $u-g$ vs $\log EW(H\alpha)$; f) $g-r$ vs $\log EW(H\alpha)$; g) $r-i$ vs $\log EW(H\alpha)$ and h) $i-z$ vs $\log EW(H\alpha)$. In all panels full (green) dots and (black) crosses are the results without and with emission lines, respectively. All cluster masses, metallicities, and ages have been included in the figure.

Table 6. Example of Johnson and SDSS colour evolution table for two mixed stellar populations. The complete table is in electronic format.

Z_o	$\log\tau_o$ yr	Z_y	$\log\tau_y$ yr	F	M_{cl} M_\odot	R_{out} pc	$\log LH_\alpha$ ers.s ⁻¹	$EW H_\alpha$ Å	V_c	U-B _c	B-V _c	V-R _c	R-I _c
0.008	8.00	0.0001	6.00	0	$1.2 \cdot 10^4$	126.45	38.81	1757.00	-10.315	-0.850	-0.011	0.736	-0.549
0.008	8.00	0.0001	6.00	1	$1.2 \cdot 10^4$	126.45	38.81	1643.81	-10.380	-0.827	-0.004	0.711	-0.509
0.008	8.00	0.0001	6.00	10	$1.2 \cdot 10^4$	126.45	38.81	1030.71	-10.838	-0.680	0.034	0.559	-0.277
0.008	8.00	0.0001	6.00	100	$1.2 \cdot 10^4$	126.45	38.81	172.46	-12.456	-0.388	0.092	0.285	0.105
0.008	8.00	0.0001	6.00	1000	$1.2 \cdot 10^4$	126.45	38.81	-39.88	-14.810	-0.290	0.108	0.202	0.214
0.008	8.00	0.0001	6.00	5000	$1.2 \cdot 10^4$	126.45	38.81	-61.54	-16.544	-0.280	0.110	0.193	0.226
0.008	8.00	0.0001	6.00	0	$2.0 \cdot 10^4$	163.68	39.03	1757.00	-10.878	-0.845	-0.007	0.726	-0.548
0.008	8.00	0.0001	6.00	1	$2.0 \cdot 10^4$	163.68	39.03	1643.60	-10.943	-0.822	-0.001	0.701	-0.508
0.008	8.00	0.0001	6.00	10	$2.0 \cdot 10^4$	163.68	39.03	1029.86	-11.397	-0.677	0.036	0.552	-0.276
0.008	8.00	0.0001	6.00	100	$2.0 \cdot 10^4$	163.68	39.03	172.05	-13.012	-0.387	0.093	0.284	0.105
0.008	8.00	0.0001	6.00	1000	$2.0 \cdot 10^4$	163.68	39.03	-39.93	-15.365	-0.290	0.108	0.202	0.214
0.008	8.00	0.0001	6.00	5000	$2.0 \cdot 10^4$	163.68	39.03	-61.55	-17.099	-0.280	0.110	0.193	0.226

Table 6. Cont. Johnson and SDSS colour evolution for two mixed stellar populations

V	U-B	B-V	V-R	R-I	g_c	u- g_c	g-r _c	r-i _c	i-z _c	g	u-g	g-r	r-i	i-z
-10.076	-1.245	0.158	0.253	0.152	-10.124	-0.010	0.424	-0.890	-0.167	-9.619	-0.499	0.009	0.030	-0.228
-10.157	-1.196	0.154	0.249	0.157	-10.177	0.015	0.405	-0.851	-0.154	-9.703	-0.443	0.004	0.024	-0.211
-10.696	-0.913	0.137	0.226	0.185	-10.567	0.182	0.285	-0.618	-0.091	-10.259	-0.114	-0.019	-0.005	-0.123
-12.425	-0.437	0.115	0.198	0.220	-12.077	0.550	0.040	-0.199	-0.011	-12.008	0.485	-0.049	-0.042	-0.017
-14.807	-0.296	0.111	0.192	0.228	-14.402	0.686	-0.044	-0.070	0.008	-14.394	0.679	-0.055	-0.051	0.007
-16.543	-0.281	0.110	0.191	0.229	-16.133	0.702	-0.054	-0.056	0.010	-16.131	0.701	-0.056	-0.052	0.009
-10.631	-1.245	0.158	0.253	0.152	-10.687	-0.001	0.414	-0.888	-0.168	-10.174	-0.499	0.009	0.030	-0.228
-10.712	-1.196	0.154	0.249	0.157	-10.740	0.024	0.396	-0.849	-0.155	-10.258	-0.444	0.004	0.024	-0.211
-11.251	-0.913	0.137	0.226	0.185	-11.128	0.188	0.279	-0.616	-0.091	-10.814	-0.114	-0.019	-0.005	-0.124
-12.980	-0.437	0.115	0.198	0.220	-12.633	0.552	0.038	-0.199	-0.011	-12.563	0.485	-0.049	-0.042	-0.017
-15.362	-0.296	0.111	0.192	0.228	-14.957	0.687	-0.045	-0.070	0.008	-14.949	0.679	-0.055	-0.051	0.007
-17.098	-0.281	0.110	0.191	0.229	-16.687	0.702	-0.054	-0.056	0.010	-16.686	0.701	-0.056	-0.052	0.009

with the number of ionising photons and SED shape, determines the ionisation parameter responsible for the emission line luminosities. These emission line luminosities are the ones included in the colour determination after weighting the luminosities (from both old and young populations) according to their relative masses.

This paper is focused on showing the importance of the emission line contributions in mixed population colours for nearby HII and starburst regions at redshift zero. The effect will be similar for more distant galaxies, where the emission line contribution to the different bands will change with redshift for the standard systems (e.g. Johnson, SDSS, etc.).

This can impact upon estimations of some M/L relationships and/or dust extinction in systems at different redshifts dominated by young ionising star forming bursts. It will also be more important at increasing redshift than at redshift zero, since the star formation becomes more violent and the mass of the young ionising population becomes larger.

When a detailed study of the photometric evolution at high-redshift is performed, it will be necessary to take into account that a large number of star-forming regions could be contributing in the different pass-bands, changing the canonical and widely accepted colour-colour theoretical diagrams for synthetic populations. This will be the object of future work in this series.

We have calculated the colours of a system composed of two populations: one older than 100 Myr ($\log\tau(\text{yr}) \geq 8.00$) and one younger than this same limit ($\log\tau < 8.00$). The stellar mass of the young population in this model grid takes the same values as in the SSP models: 0.12, 0.20, 0.40, 0.60, 1.0, 1.5 and $2.0 \times 10^5 M_\odot$. For each model or composite system, we assume an old stellar population with a mass on the zero time main sequence defined by a

factor $F = M_{old}/M_{young}$. We have taken 6 possible values for this grid, $F=0, 1, 10, 100, 1000$ and 5000. Colours are computed by using the total luminosity emitted by both the old population and the young stellar population, including the emission lines contribution and the nebular continuum, as we show in the previous sections.

We have obtained a table for each old stellar population defined by its age and metallicity, where all possible combinations with the young stellar population (scanning the grid in mass, age and metallicity of the young cluster) are included. We show in Table 6 an example of this type of result. The complete set of tables for all ages and metallicities of the old stellar population are available in electronic format (and they are also available at the POPSTAR web page, <http://www.fractal-es.com/PopStar>). Different columns in Table 6 are: column 1 and 2, the metallicity and age of the old population; columns 3 and 4, the metallicity and age of the young cluster; column 5, the factor F or mass ratio between old and young populations; column 6, the young population's mass; column 7, the outer radius (or observed photometrical radius) of the region in pc; column 8, the logarithm of the luminosity of H_α in erg.s^{-1} ; column 9, the equivalent width of H_α , $EW(H_\alpha)$, in Å; columns 10 to 14 are the magnitude V and colours U-B, B-V, V-R and R-I respectively, corresponding to Johnson system, and in which the emission lines contribution has been included, columns 15 to 19 are the same quantities than in columns 10 to 14 but without the emission line contribution (canonical system). Similarly, columns 20 to 24 are the magnitudes g and colours u-g, g-r, r-i and i-z (of the SDSS system) including the emission lines contribution while columns 25 to 29 are the same quantities without the emission line effect.

4.1 Colour Evolution

Fig 15 shows two examples of these mixed populations. We show the time evolution of the same colours as in the previous SSP figures for two cases: Case (1) in the four top panels, we consider a stellar system composed of an old stellar population of 10 Gyr and $Z = 0.0001$ plus a young stellar population of $10^5 M_{\odot}$ and $Z = 0.0004$. The figure shows the colour evolution with the young cluster age, ranging from 0 to 20 Myr. Case (2) in the four bottom panels considers the mixing of an old stellar population of 10 Gyr and $Z = 0.004$ with a young cluster mass of $10^5 M_{\odot}$ and metallicity of $Z = 0.008$. In all cases the dashed lines are the colours calculated without the emission line contribution, while the solid lines correspond to the total colour including this contribution. Different colours indicate different F values, ranging from 0 (black, and meaning a pure young population) to 5000 (red, meaning a quite important mass contribution of the underlying old component, in this case $5 \times 10^8 M_{\odot}$ since the young cluster mass is $10^5 M_{\odot}$). These F values and the legend have been labelled in the V-R vs R-I diagrams. The higher the value of F , the smaller the emission lines impact on the integrated colour, as expected. In the plots, larger differences between dashed and solid lines can be appreciated for small F values while both lines are almost coincident for large F values. The cases with $F = 0$ correspond to a pure young population and therefore to the case discussed in §3 of this paper. It can also be seen that as the young population evolves, the contribution of the lines tends to disappear, and the dashed and solid lines tend towards coincidence.

When F is in the range 1 (magenta line) to 10 (blue line), the old population contributes in a small proportion and the young population dominates the system. In these cases, colours U-B, V-R and R-I for the first evolutionary phases of the young population (age < 5 Myr) present a behaviour close to the one with F around 100 and no-emission lines contribution (green dashed lines). It means that using a mixture of two populations without taking into account the emission line contribution, can lead to a misinterpretation, by assigning a stronger contribution of the underlying population than the actual one. Thus, for this particular example, the error determination can be as high as one order of magnitude in the F value, implying a similar error for the determination of the mass of the underlying population (assuming that we can constrain the young population mass through other photometric values, like the H_{α} luminosity).

Only the colour B-V and somehow U-B seem to provide similar estimations for the old population's age, regardless of the models used (with or without emission lines). A similar behaviour is observed in the Case (2), displayed in the four bottom panels, which indicates that this effect is quite independent of the metallicity for these examples. Of course, these conclusions can change for other combinations of metallicities and for younger ages of the old population. The potential confusion will become larger when a stronger starburst is overlapping with an intermediate-age population. We have plotted this extreme case with a very old underlying population to demonstrate that even in this system we can find important differences in the inferred physical properties when using canonical models instead of the ones with the emission line contribution.

Fig. 16 shows the same example of mixed populations, but for SDSS colours. The plots for case (1) show the same effect of possible misinterpretation in the colours u-g, g-r, and r-i when using uncontaminated colours instead of the ones including the emission line contribution. Again, differences larger than one order of magnitude in the burst strength can be inferred. From the lower panels (case 2),

all the colours, and especially r-i and i-z, would lead to misinterpretation. We cannot provide plots for the whole range of age, mass, and metallicity of the contributing populations, but given a specific set of photometric observations, a good representation of the reality may be obtained by fitting the different parameters to the theoretical models, following for example a mean square error (MSE) as a measure of estimator quality. We provide the complete set of tables and models in electronic format to allow these computations.

4.2 Colour-Colour Diagrams

The same mix of stellar populations as before are represented in Fig.17 and Fig.18 as colour-colour diagrams. As in Fig. 15 and Fig. 16, different colour lines represent different ratios in mass, F , between old and young stellar populations. Thus red lines give the colour-colour results when the old stellar population dominates in mass, with a value of $10^8 M_{\odot}$ over the young one of $10^5 M_{\odot}$ while the black lines represent the evolution of a simple young stellar population without underlying population. All the other colours (orange, green, blue and magenta) represent intermediate cases.

The dashed lines are the results without the emission line contribution while the solid lines show our results including the emission line contamination. In these figures, the model results given by the solid lines (emission lines included) can be bluer or redder, compared to the models of the dashed-lines (no emission lines). This will depend also on F . For a given value of F , models on the solid lines (with lines) will be close or far from the canonical solid line (they can be placed also on an orthogonal line) depending on the age of the young population as discussed in §3. Our results predict a large dispersion among the observational values when plotting them in colour-colour plots, explaining in a natural way this fact. Previous work often proposed a reddening excess due to dust to explain the discrepancy between the synthetic colours and the observed ones.

4.3 Colours vs H_{α} Equivalent Widths

Finally, Fig. 19 and Fig. 20 show the synthetic colours for the same combinations of stellar populations described in the previous subsections vs the equivalent width of H_{α} with the same meaning of colours and line types for Johnson and SDSS colours respectively. As we have seen before, the emission lines do colours bluer or redder, and therefore the resulting solid lines fall in a different region than the dashed lines (canonical models without the emission line contribution) for a given value of the H_{α} equivalent width. In the example corresponding to Fig. 19 Case 1 (upper panels) B-V (panel b) shows that differences between solid and dashed lines are small, so that estimations based on this type of plot would be similar using the colours with or without emission lines. However this is not the case for the other colours (panels a, c and d for U-B, V-R and R-I respectively) for which we suggest that the colours including emission lines are redder (for U-B and V-R) or bluer (for R-I) than the ones synthesised without this contribution. A similar behaviour is found in Case 2 (lower four panels).

As in previous figures, different colour lines correspond to different values of F , from 0 (black, pure young population) to 5000 (red, with a strong mass contribution of the underlying population). For $F = 0$ models (single population), the evolution shows blue colours and high values of $EW(H_{\alpha})$ for the younger clusters, and a progressively decrease of $EW(H_{\alpha})$ and colour reddening as far as the cluster evolves. Models on dashed lines do not present simultaneously red colours and high values of $EW(H_{\alpha})$ as observed in HII

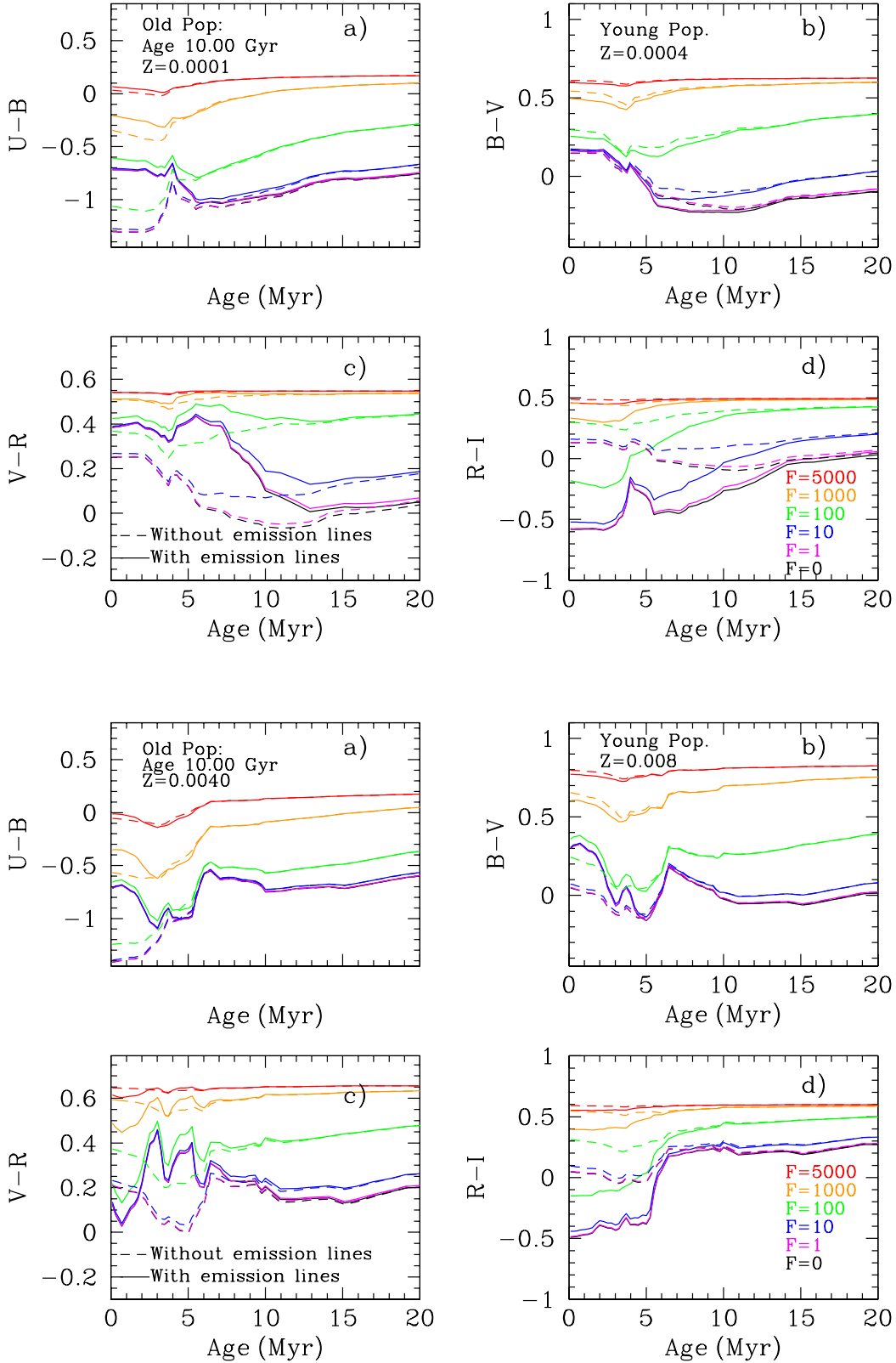


Figure 15. Examples of Johnson colour evolution with a young cluster age in a mixed population. This is composed of an old 10 Gyr underlying cluster plus a young burst ($\tau < 20$ Myr and clear H_α emission). Each colour represents a different mass contribution of the old population to the young burst (F , being mass-old / mass-young) as labelled. Synthetic colours with and without the emission lines contribution are plotted as solid and dashed lines respectively. Two metallicity cases have been chosen as examples: top panels use $Z = 0.0001$ and $Z = 0.0004$ for old and young populations, while bottom panels get $Z = 0.004$ and $Z = 0.008$, as labelled in the plots.

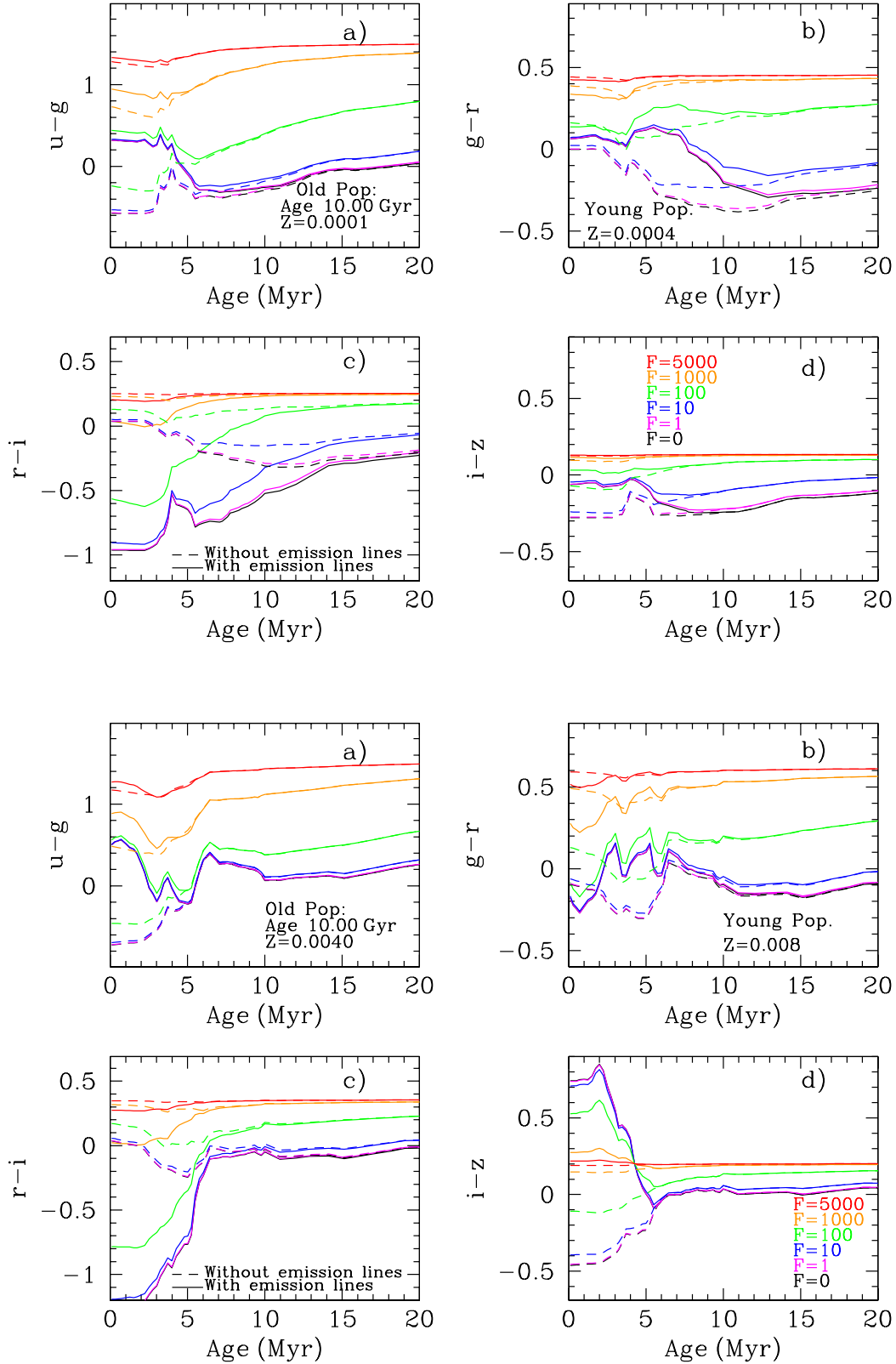


Figure 16. Examples of SDSS colour evolution with a young cluster age for a mixed population. This is composed by an old 10 Gyr underlying cluster plus a young burst (Age $\tau < 20$ Myr and clear H_{α} emission). Each colour represents a different mass contributions of the old population to the young burst (F , being mass-old / mass-young) as labelled. Synthetic colours with and without the emission lines contribution are plotted as solid and dashed lines respectively. Two metallicity cases have been chosen as examples: top panels use $Z = 0.0001$ and $Z = 0.0004$ for old and young population, while bottom panels get $Z = 0.004$ and $Z = 0.008$, as labelled in the plots.

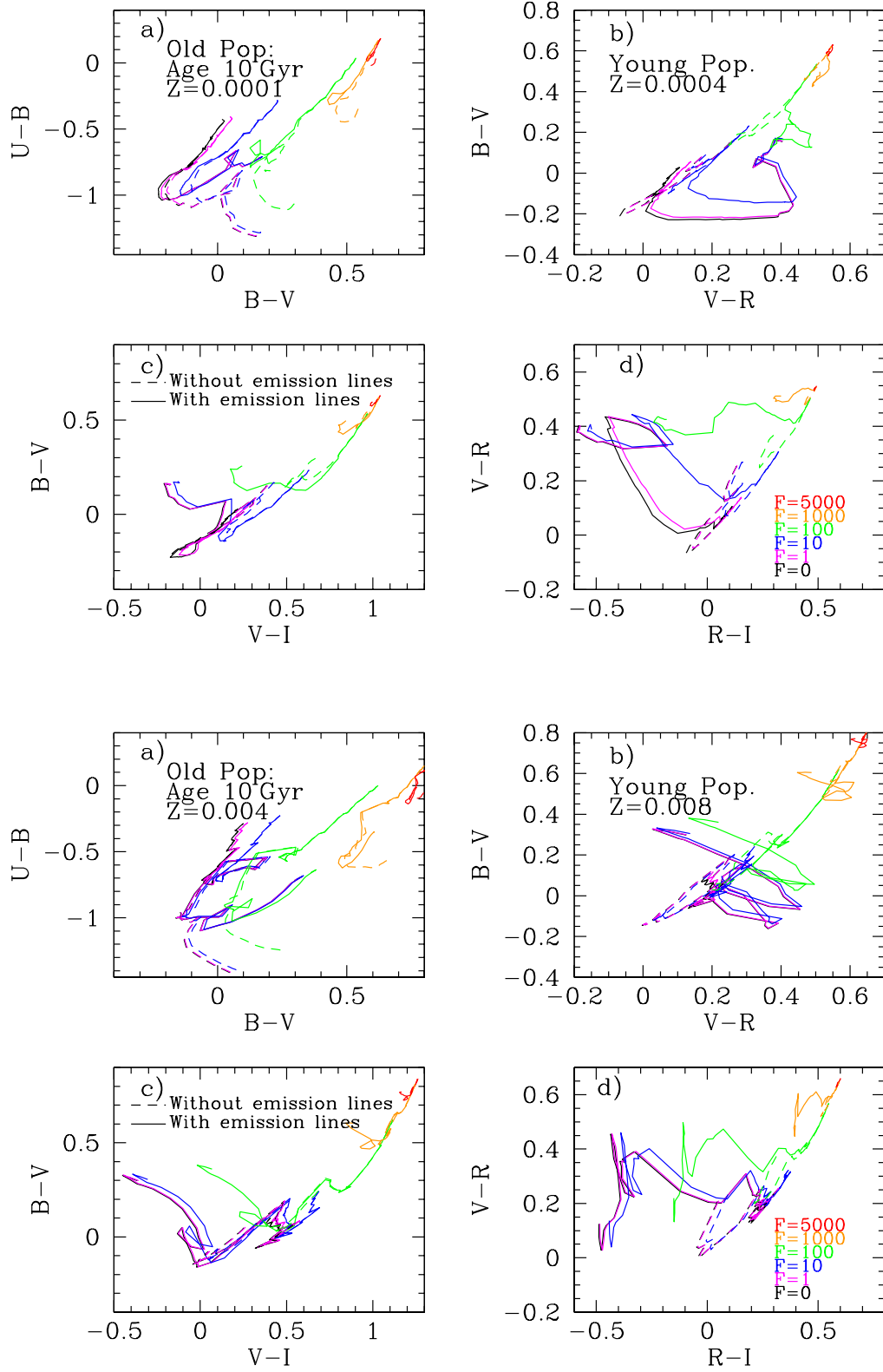


Figure 17. Examples of Johnson colour-colour evolution for a mixed population. This is composed by an old 10 Gyr underlying cluster plus a young burst ($\tau < 20$ Myr and clear H_{α} emission). Different coloured lines represent a different mass contribution of the old population to the young burst (F, being mass-old / mass-young). Synthetic colours with and without the emission lines contribution are plotted as solid and dashed lines respectively. Two metallicity cases have been chosen as examples: top panels use $Z = 0.0001$ and $Z = 0.0004$ for old and young population respectively while bottom panels get $Z = 0.0004$ and $Z = 0.0008$, as labelled in the plots.

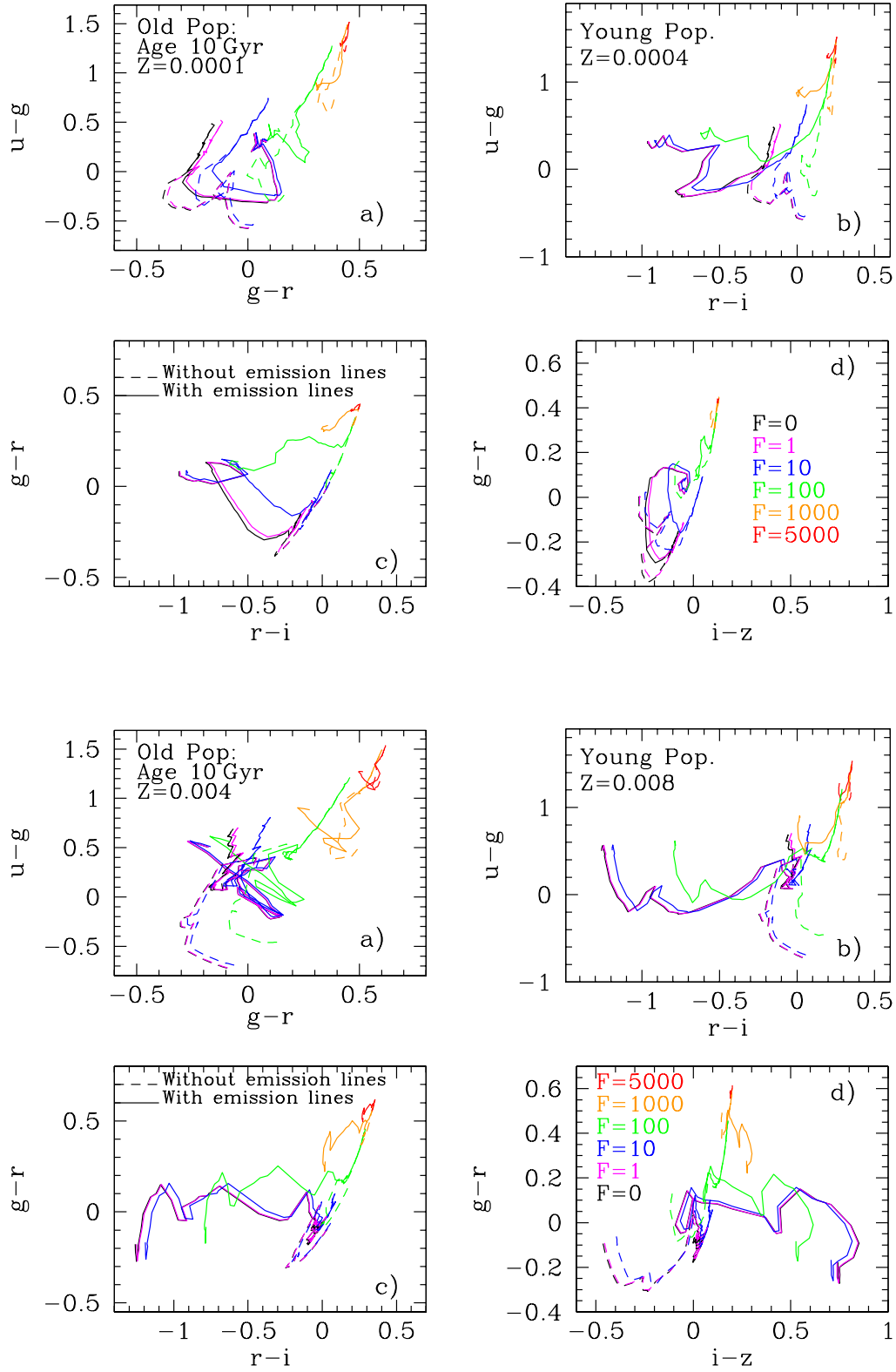


Figure 18. Examples of SDSS colour-colour evolution for a mixed population. This is composed by an old 10Gyr underlying cluster plus a young burst ($\tau < 20$ Myr and clear $H\alpha$ emission). Different coloured lines represent a different mass contribution of the old population to the young burst (F , being mass-old / mass-young). Synthetic colours with and without the emission lines contribution are plotted as solid and dashed lines respectively. Two metallicity cases have been chosen as examples: top panels use $Z = 0.0001$ and $Z = 0.0004$ for old and young population respectively while bottom panels get $Z=0.0004$ and $Z=0.0008$, as labelled in the plots.

galaxies for example. This is not the case for the models with the emission lines, in which we can find red colours and high values of $EW(H_\alpha)$ in the range of several hundreds or even few thousands, at early ages, without the need for interpreting this as a dust excess.

4.4 Comparison with Observational Data

In this section we test our models to see if they can reproduce the photometric observations from star forming regions where it is already proved that at least a young and an old stellar population exists there. We have analysed the HII region data of Martínez-Delgado et al. (2009), where photometry exists for a well-observed sample of Blue Compact Dwarf (BCDs) galaxies with spectroscopic metallicity determinations. This makes the sample suitable to compare with our models, in order to see if our predicted colours for mixed populations can reproduce these data. We have plotted different synthetic photometric parameters versus the equivalent width of H_α , which is a proxy of the age, together with observations of HII regions for two galaxies: III Zw 107 and III Zw 102 in Figs. 21 and 22, respectively. In both figures panels a) to d) plot the synthetic colours U-B, B-V, V-R and R-I respectively. Panel e) uses the H_α luminosity and panel f) the photometric radius of the HII region, R_{out} .

Observed regions in Figs. 21 and 22 correspond to data for the galaxies III Zw 107, and III Zw 102, respectively, plotted as red crosses. The metallicity for the first galaxy estimated from its oxygen abundance (itself derived using optical emission lines) is $12 + \log [O/H] = 8.23$, equivalent to $Z \sim 0.004$ (López-Sánchez & Esteban, 2010). This metallicity is also consistent with the appearance of WR features in spectroscopy observations. Similarly for III Zw 102, the estimated abundance (from spectroscopic oxygen abundances from 3D spectroscopy) is $12 + \log [O/H] = 8.49$ (Cairós et al., 2012), equivalent to $Z \sim 0.008$.¹

In these two galaxies used as examples it is impossible to explain the observed colours without the existence of an older underlying stellar population, as can be seen in Fig. 21 and Fig. 22, where the synthetic colours for the case of a SSP ($F = 0$) of a metallicity as the one estimated from the emission lines as given before, without the contribution of the emission lines (cyan open dots) and with the emission lines (black full dots), cannot reproduce the observed colours. We can see that neither of the two set of models can reproduce the observations. In Fig 21 and and Fig. 22, we cannot find any solution for colours U-B (panel a), B-V (panel b), V-R (panel c) and R-I (panel d), when data are available, and neither is it possible to find a population able to simultaneously fit the colours and the H_α equivalent width.

The presence of such an underlying old population is widely accepted in BCGs, as the case of III Zw107 and III Zw102. Although their low metallicity and the very young stellar populations led some time ago to the proposal that these systems could be suffering their first burst of star formation (Sargent & Searle, 1970) more recent observations point to these galaxies seem to be not as young as it was originally thought. Photometric observations indicate that they host stellar populations, reaching in some cases a few Gyr (Telles et al., 1997; Legrand, 2000; Tolstoy, 2003; Cairós et al., 2003; van Zee et al., 2004; Thuan & Izotov, 2005). There is now wide agreement about the existence of underlying populations with ages of several Gyr in BCGs and/or HII galaxies. Even the

most metal-poor galaxy known, I Zw18, the best candidate to primordial galaxy, has started forming stars earlier than ~ 1 Gyr old (Annibali et al., 2013). For this reason, the fit of a mixed population to the observed data, might improve the result.

Therefore we have selected among all the mixed stellar populations models computed in our grid and described in the previous section, those ones whose colours and equivalent width $EW(H_\alpha)$ can fit the observations within the error bars. To do that we have performed a chi-square fit of our mixed models in which the metallicity of the young stellar population, Z_{young} , is equal to the estimated one by the emission lines as given before. The yellow region in each figure shows the results of this fit. These results represent all possible combinations of Zold+Age-old+Age-young able to reproduce the data within errors. It is clear that there are solutions to the data.

As an example we also plot in Fig 21 the evolution with the age of the young population for one of these combinations or mixed stellar populations, which has a young stellar mass of $2 \times 10^5 M_\odot$, and $Z = 0.004$ with one 6 Gyr old with $Z = 0.004$ and with two possible values for mass contributions: $F = 1000$ (dark blue lines) and $F = 5000$ (orange lines). Solid lines represent models including emission lines while dashed lines are models without this contribution. We see that the three observed regions are better fit by the model with $F = 1000$. In panels e) and f) we show the same yellow region. Panel e) shows that two of the observed regions have H_α luminosities larger than those of the plotted models. This is likely due to the fact that our grid does not include cluster masses larger than $2 \times 10^5 M_\odot$. At least (although obviously the interpretation would be different if other IMF is used) we can put a lower limit for the mass of these HII regions.

Similar to Fig. 21 we have plotted Fig. 22 with our models and observed data of star-forming regions in III Zw102. Again, most of observational points cannot be fit by the SSP. We represent the region of selected mixed models as yellow points as before. This region is not valid for all data and some observed parameters are not reproduced with our current set of models. Perhaps larger F factors are necessary to fit these very red colours in regions where $EW(H_\alpha)$ is still present, or maybe the averaged abundance $Z = 0.008$ is not representative for all HII regions. Following the results of panel e), the young stellar population mass of these regions should be smaller than our lowest limit, $10^4 M_\odot$. This would also explain the values of the observed radii also being smaller than the predicted ones. It is necessary to remain that the chi-square fit is performed using only the data of panels a) to d), not e) nor f). Nevertheless, the two-population mixed model is also a simplification since some of the regions are not spatially resolved and can contain more than two stellar populations with different ages. It has to be noticed that the worse fitting found in the colours U-B and B-V is fully consistent with the strong dust absorption found in this galaxy, as reported by Cairós et al. (2012)

Fig. 21 and Fig. 22 show that our models can fit real data of photometric observations of HII regions, obtaining the metallicity and the age for both the young and the old populations and reproducing several colours simultaneously when SSPs cannot do it. Moreover, the inclusion of emission lines in the models is needed to reproduce simultaneously all the colours in the two selected galaxies. It has to be notice that the two galaxies have very different values of the metallicity, which has been spectroscopically confirmed by different papers in the literature.

Finally, we plot in Fig. 23 data obtained by Mayya (1994) for a sample of HII regions in external galaxies. Each galaxy's regions are plotted with a different code as labelled in panel b). Only two

¹ Solar abundance in our models is taken as: $12 + \log [O/H] = 8.67$, equivalent to $Z = 0.015$, (Asplund et al., 2009).

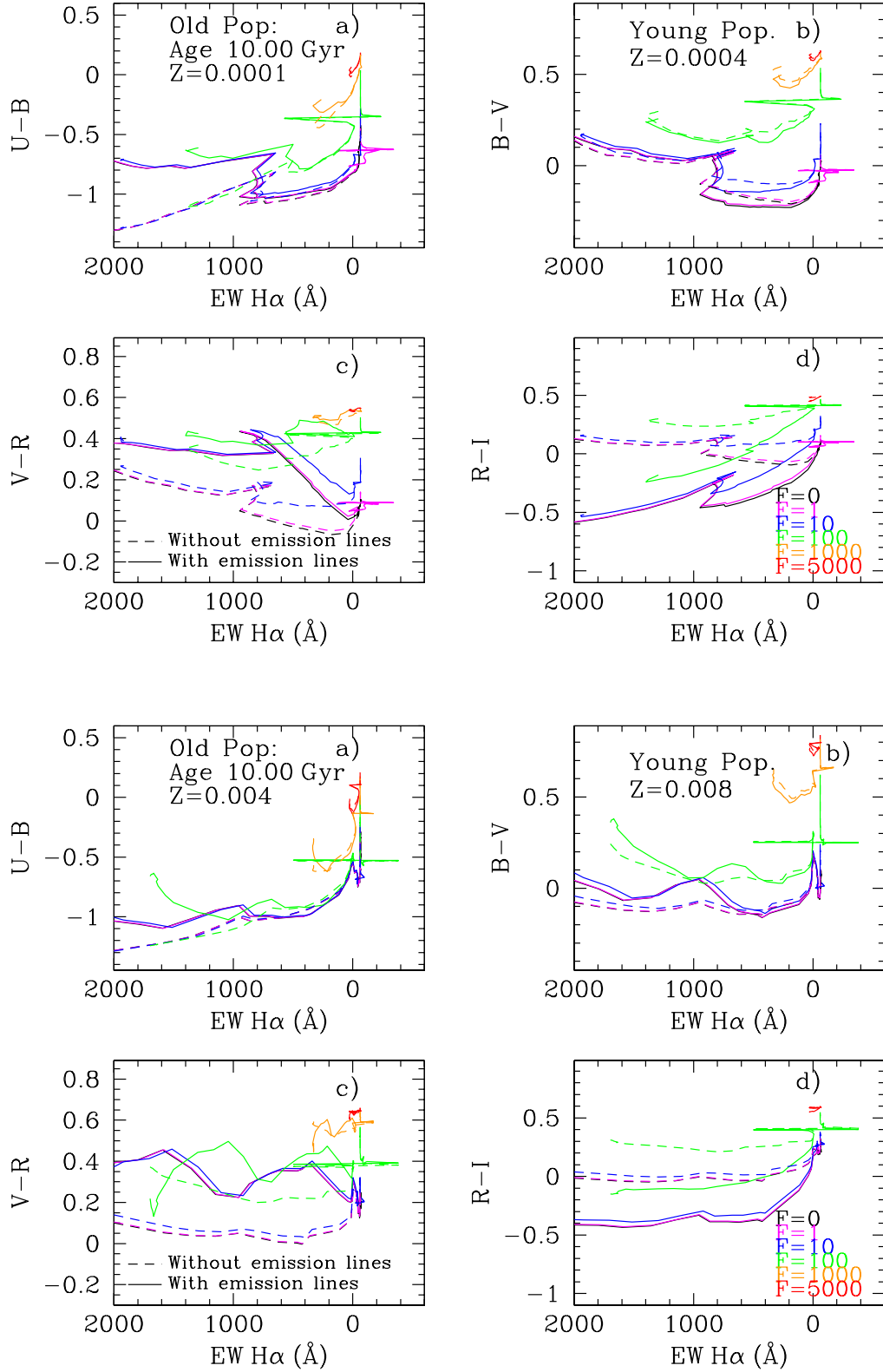


Figure 19. Examples of different Johnson colours - as labelled in the panels - plotted against the Equivalent Width of $H\alpha$ in emission for a mixed population. This is composed by an old 10 Gyr underlying cluster plus a young burst ($\tau < 20$ Myr and clear $H\alpha$ emission). Each coloured line represents a different mass contribution of the old population to the young burst (F, being mass-old / mass-young). Synthetic colours with and without the emission lines contribution are plotted as solid and dashed lines respectively. Two metallicity cases have been chosen as examples: top panels use $Z = 0.0001$ and $Z = 0.0004$ for old and young population respectively while bottom panels get $Z = 0.004$ and $Z = 0.008$, as labelled in the plots.

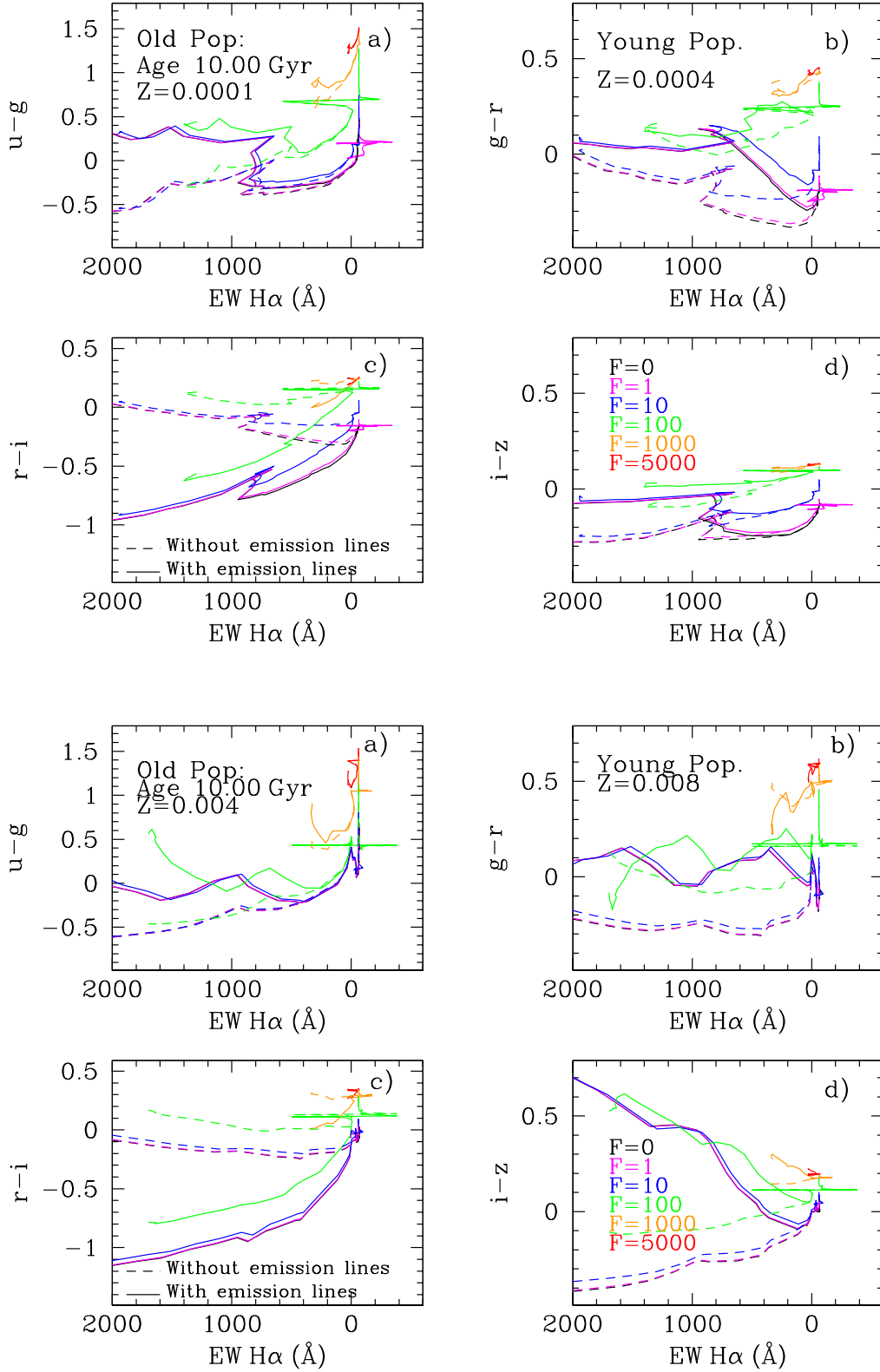


Figure 20. Examples of different SDSS colours - as labelled in the panels - plotted against the Equivalent Width of H α in emission for a mixed population. This is composed by an old 10 Gyr underlying cluster plus a young burst ($\tau < 20$ Myr and clear H α emission). Each coloured line represents a different mass contribution of the old population to the young burst (F, being mass-old / mass-young). Synthetic colours with and without the emission lines contribution are plotted as solid and dashed lines respectively. Two metallicity cases have been chosen as examples: top panels use $Z = 0.0001$ and $Z = 0.0004$ for old and young population respectively while bottom panels get $Z = 0.004$ and $Z = 0.008$, as labelled in the plots.

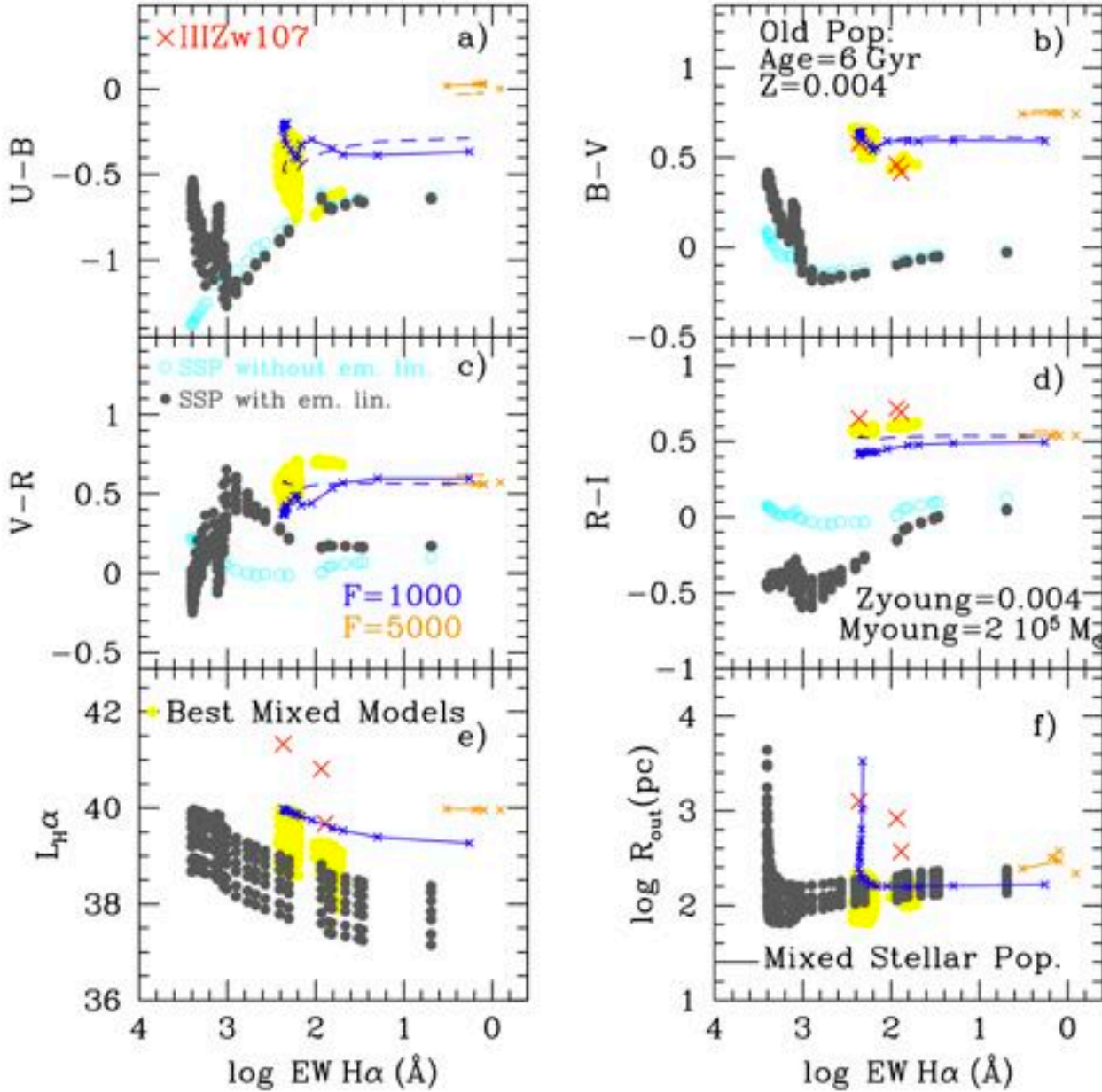


Figure 21. Colours U-B, B-V, V-R and R-I, logarithm of $H\alpha$ luminosity (erg.s^{-1}) and logarithm of the HII region radius, R_{out} (in pc), vs $EW(H\alpha)$. Observed data for star-forming regions in the galaxy III Zw 107 (Martínez-Delgado et al. (2009)) are plotted as red crosses. SSPs models with $Z = 0.004$ are shown with open (cyan) and full (black) dots. The yellow region is the locus of models with $Z_{young} = 0.004$, the estimated metallicity from visible spectroscopy of the observed star-forming regions, that are able to reproduce simultaneously the observed colours and $EW(H\alpha)$. From these 2-population mixed models we have selected those ones with an old population of the same metallicity, $Z = 0.004$, and 6 Gyr old and two values of F , $F = 1000$, whose evolution with the young population age is plotted as a blue line, and $F = 5000$, plotted as an orange line, to show as example the evolution of a mixed population.

colours and the equivalent width $EW(H\alpha)$ are available for this sample. In this figure, we plot as an example the model with $Z = 0.02$ for the young stellar population and $Z = 0.004$ for the old one, with an age of 10 Gyr. Different factors F are shown with lines of different colours as labelled in the plot. We see that most of data could need values of F in the range 100 – 1000, with only some exceptional points out of the region defined by these two lines. We might perform a similar selection technique to see which models

are the best ones to fit these data, or use a mean square error (MSE) analysis to derive the most appropriate models for each galaxy or HII region, but this is beyond the scope of this work. What we want to show with this figure is that mixed population models including emission lines can reproduce the observations of star-forming regions, while SSPs cannot, and models without emission lines do not offer the same result, and ultimately result in a misinterpretation of the physical stellar population parameters.

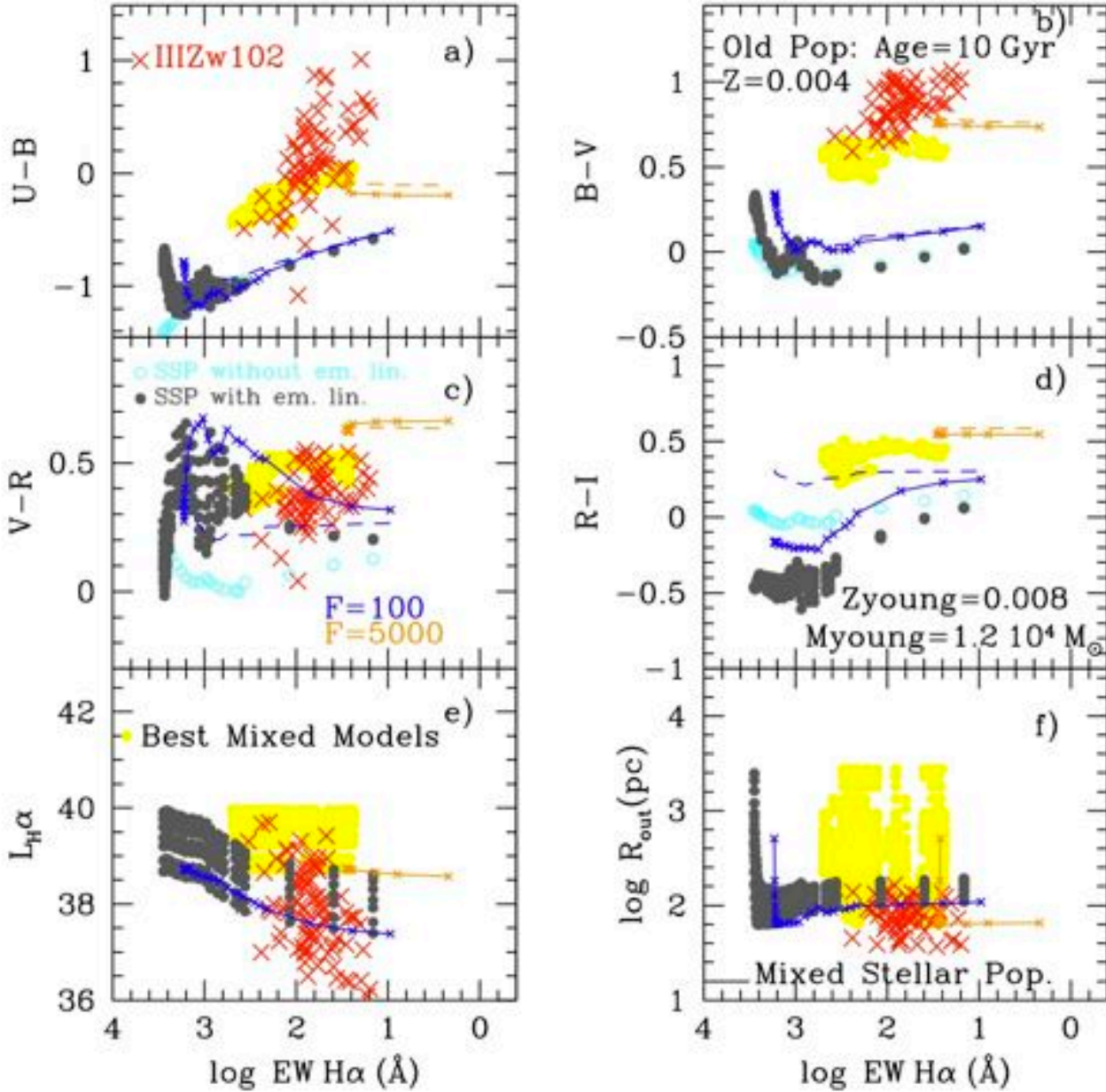


Figure 22. Colours $U-B$, $B-V$, $V-R$ and $R-I$, logarithm of $\text{H}\alpha$ luminosity (in erg.s^{-1}) and logarithm of the HII region radius, R_{out} (in pc), vs $\text{EW}(\text{H}\alpha)$. Observed data for star-forming regions in the galaxy III Zw 102 (Martínez-Delgado et al. (2009)) are plotted as red crosses. SSPs models with $Z = 0.008$ are shown with open (cyan) and full (black) dots. The yellow region is the locus of models with $Z_{\text{young}} = 0.008$, the estimated metallicity from visible spectroscopy of the observed star-forming regions that are able to reproduce simultaneously the observed colours and $\text{EW}(\text{H}\alpha)$. From the 2-population mixed models we have selected those ones with an old population of $Z = 0.004$ and 10 Gyr old and two values of F , $F = 100$, whose evolution with the young population age is plotted as a blue line; and $F = 5000$, plotted as an orange line, to show as example the evolution of a mixed population.

5 CONCLUSIONS

- We have calculated the same grid of magnitudes and colours as in Paper I with the PopStar code, but now incorporating the contribution from emission lines, using for that the intensities obtained in our Paper II, for a large grid of young stellar ionising clusters. We provide tables with uncontaminated and contaminated colours.

- Broadband filter magnitudes are contaminated by the emission

lines coming from ionising nebulae surrounding young stellar clusters. This contamination modifies the magnitudes (ranging from 0.2 to 1.5 mag depending on the filter) in the visible and near-infrared bands. Colours $U-B$, $B-V$, $V-R$ and $R-I$ are modified by a value between 0.2 and 0.8 mag depending on the colour and on the metallicity of the stellar population. Similar results are found in SDSS filters and should be found in other photometric systems.

- The synthetic contaminated colours for SSPs in the colour-

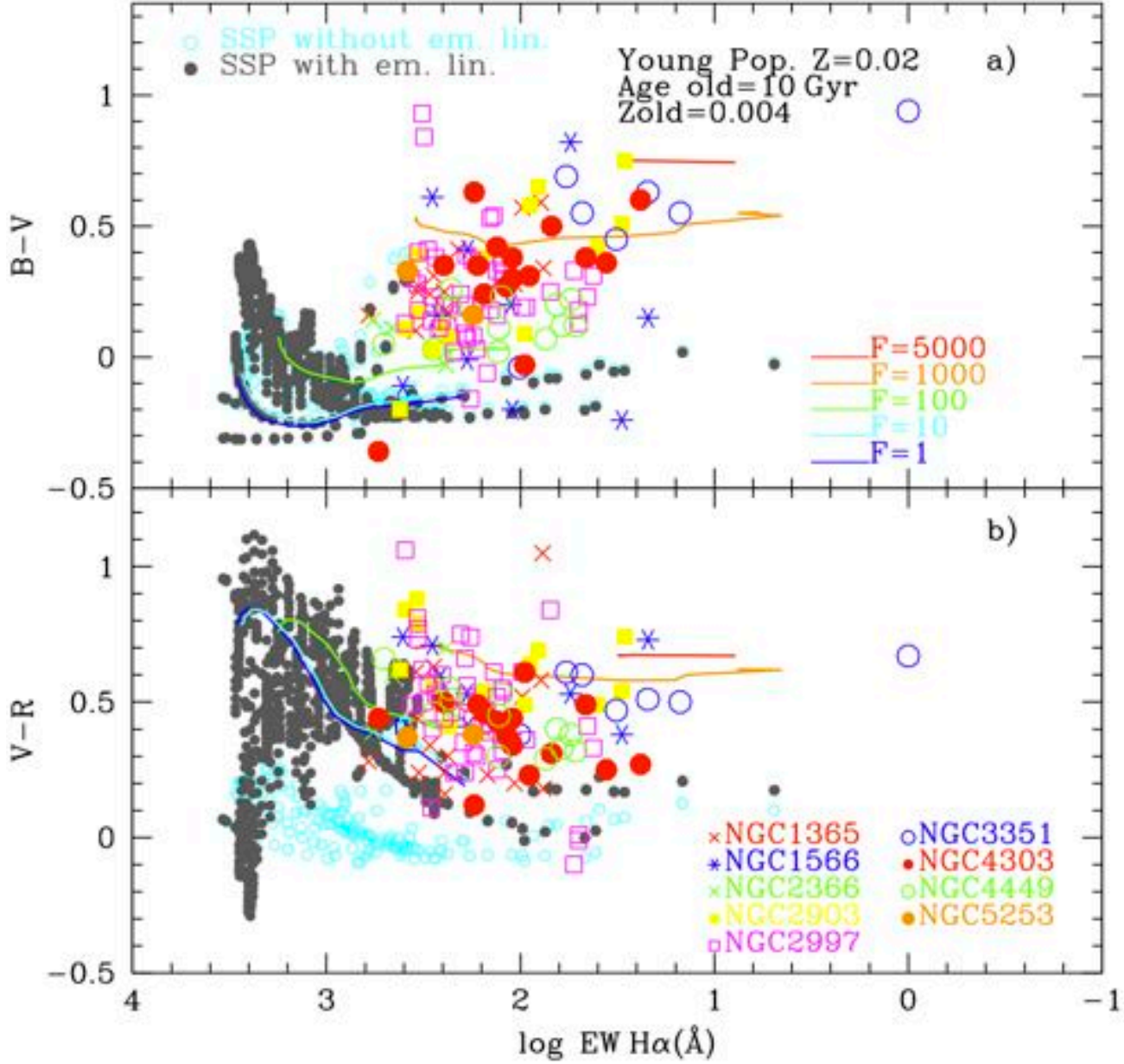


Figure 23. Colours $B-V$ and $V-R$ vs $\text{EW}(H\alpha)$. Observed data are from Mayya (1994) for HII regions located in different galaxies as labelled in the lower plot. Two mixed populations, an old one with $Z = 0.004$ and 10 Gyr old and another younger one with $Z = 0.02$, and different ages over the evolutionary sequence, are represented as solid lines with different colours following the value of F as labelled in the upper diagram. We can see that models could reproduce the observations.

colour diagrams fall outside the standard canonical sequence shown by the uncontaminated colours or those obtained for old stellar populations. In many cases they show orthogonal sequences to those ones.

- We have also computed other photometric parameters, such as $H\alpha$ and $H\beta$ luminosities, equivalent widths of $H\alpha$ and $H\beta$ and radii of the corresponding HII regions.

- The equivalent widths for $H\alpha$ and $H\beta$ do not depend only on the age. They also depend on the metallicity of the stellar population. The $\text{EW}(H\alpha)$ decreases with age until 5-7 Myr if $Z > 0.004$.

For lower metallicities, $\text{EW}H\alpha$ maintains positive values until 15-18 Myr. The same occurs with $H\alpha$ and $H\beta$ luminosities, which have high values until ~ 20 Myr for the lowest metallicities ($Z < 0.004$).

- The outer calculated radii of low metal HII regions are quite large compared with those observed at intermediate metallicities. Since these regions are not present in the observational samples, and taking into account that they must show high $H\alpha$ luminosities too, we need to consider the impact of observational selection effects that might be able to lead the production of biased HII region samples.

- An evolutionary track in the plane R_{out} - $L(H_\alpha)$ shows that the radius of the region increases when the H_α luminosity decreases. However a positive correlation $L(H_\alpha) - R_{out}$ arises when all stellar cluster masses and metallicities are drawn together, so the observed correlation and its dispersion may be explained by a mix of stellar clusters of different ages, metallicities and masses.

- We have also computed a grid of models where a recent ionising burst is mixed with an underlying and older host stellar population in different proportions. We give magnitudes and colours for these mixed stellar populations. In some cases contaminated colours with a low contribution of an old stellar population are similar to the uncontaminated colours with a high proportion of old population. This is important when interpreting observations from regions where there exists an underlying stellar population, since the wrong ratio F will be estimated if the uncontaminated colours, instead the ones contaminated by emission lines, are used when comparing observational data and models to derive physical properties of the stellar populations.

- Other photometric parameters have also been given for each mix of stellar populations as before: H_α and H_β luminosities, equivalent widths for H_α and H_β and radii of the corresponding HII regions. This allows one to compare the observed radii of HII regions, their colours, and their equivalent widths of H_α with the models. We have checked with some test cases that our models can reproduce photometric observational data and that it is possible to find the best mix of stellar populations able to fit simultaneously several photometrical observations.

- All these models have been computed at redshift zero but detailed models will be available soon for higher redshifts, taking into account their shift with z and the contribution to the different standard filters in the visible and near-IR.

6 ACKNOWLEDGMENTS

This work has been partially supported by FRACTAL SLNE, DG-ICYT grant AYA2007-67965-C03-02, AYA2010-21887-C04-02 and AYA2010-21887-C04-03, and partially funded by the Spanish MEC under the Consolider-Ingenio 2010 Program grant CSD2006-00070: First Science with the GTC (<http://www.iac.es/consolider-ingenio-gtc/>). Also, partial support from the Comunidad de Madrid under grant CAM S2009/ESP-1496 (AstroMadrid) is grateful. An anonymous referee is acknowledged by useful comments that improved this work. We would like to thank Dr. B.K. Gibson warmly for his help reviewing this manuscript and correcting the English version. We would like to thank the anonymous referee for suggestions that improved this paper.

REFERENCES

- Annibali F., et al. 2013, AJ, submitted (arXiv 1303.3909)
- Asplund M., Grevesse N., Sauval A. J., Scott P., 2009, ARA&A, 47, 481
- Atek H., et al., 2011, ApJ, 743, 121
- Bressan A., Granato G. L., Silva, L., 1998, A&A, 332, 135
- Cairós L. M., García-Lorenzo B., Caon N., Vílchez J. M., Papaderos P., Noeske K., 2003 Ap&SS, 284, 611
- Cairós L. M., Caon N., García-Lorenzo B., Kelz A., Roth M., Papaderos P., Streicher O., 2012 A&A, 547, A24
- Castor J., McCray R., Weaver R., 1975, ApJ, 200, L107
- Ferland G. J., Korista K. T., Verner D. A., Ferguson J. W., Kingdon J. B., Verner E. M., 1998, PASP, 110, 761
- Ferreiro D. L., Pastoriza M. G., 2004, A&A, 428, 837
- Gibson B. K., 1994, JRASC, 88, 383
- Girardi L., Bertelli G., Bressan A., Chiosi C., Groenewegen M. A. T., Marigo P., Salasnich B., Weiss A., 2002, A&A, 391, 195
- Girardi L., Grebel E. K., Odenkirchen M., Chiosi C., 2004, A&A, 422, 205
- Grevesse N., Sauval A. J., 1998, SSRv, 85, 161G
- Hakobyan A. A., Petrosian A. R., Yeghazaryan A. A., Boulesteix J., 2007, Ap, 50, 426
- Hillier D. J., Miller D. L., 1998, ApJ, 496, 407
- Lejeune Th., Cuisinier F., Buser R., 1997, A&AS, 125, 229
- Legrand F., 2000 A&A, 354, 504
- López-Sánchez Á. R., Esteban C., 2008, A&A, 491, 131
- López-Sánchez Á. R., Esteban C., 2010, A&A, 517, 85
- Martín-Manjón M. L., Mollá M., Díaz A.I. & Terlevich R. 2008, MNRAS, 385, 854
- Martín-Manjón M. L., García-Vargas M. L., Mollá M. & Díaz A.I. 2010, MNRAS, 403, 2012 (Paper II)
- Martínez-Delgado, I. et al. 2009, PhD, private communication
- Mayya Y. D., 1994, AJ, 108, 1276
- Mollá M., García-Vargas M. L., Bressan A., 2009, MNRAS, 398, 451 (Paper I)
- Pauldrach A., Hoffmann T.L., Lennon M., 2001, A&A. 375, 161
- Rauch T., 2003, A&A 403, 709
- Reines A. E., Nidever D. L., Whelan D. G., Johnson K. E., 2010, ApJ, 708, 26
- Salpeter, E. E., 1955, ApJ, 121, 161
- Sargent W. L. W., Searle L., 1970 ApJ, 162, L155
- Smith L., Norris R., Crowther P., 2002, MNRAS, 337, 1309
- Smith J. A., Tucker, D.L., Kent, S., Richmond, M.W., et al. 2002, AJ, 123, 2121
- Telles E., Melnick J., Terlevich R., 1997 MNRAS, 288, 78
- Tenorio-Tagle G., Silich S. A., Kunth D., Terlevich E., Terlevich R., 1999, MNRAS, 309, 332
- Thuan T. X., Izotov Y. I., 2005 ApJ, 627, 739
- Tolstoy E., 2003, Ap&SS, 284, 579
- van Zee L., Barton E. J., Skillman E. D., 2004, AJ, 128, 2797